Article

Synthesis, Structure Determination, and Spectroscopic/Computational Characterization of a Series of Fe(II)–Thiolate Model Complexes: Implications for Fe–S Bonding in Superoxide Reductases

Adam T. Fiedler, Heather L. Halfen, Jason A. Halfen, and Thomas C. Brunold

J. Am. Chem. Soc., **2005**, 127 (6), 1675-1689• DOI: 10.1021/ja046939s • Publication Date (Web): 19 January 2005

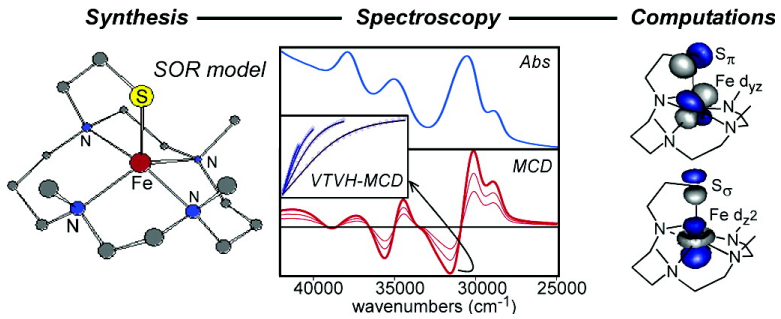

More About This Article

Additional resources and features associated with this article are available within the HTML version:

- Supporting Information
- Links to the 8 articles that cite this article, as of the time of this article download
- Access to high resolution figures
- Links to articles and content related to this article
- Copyright permission to reproduce figures and/or text from this article

View the Full Text HTML

J|A|C|S
ARTICLES
Published on Web 01/19/2005

Synthesis, Structure Determination, and Spectroscopic/Computational Characterization of a Series of Fe(II)−Thiolate Model Complexes: Implications for Fe−S Bonding in Superoxide Reductases

Adam T. Fiedler,[‡] Heather L. Halfen,[†] Jason A. Halfen,*[,†] and Thomas C. Brunold*[,‡]

Contribution from the University of Wisconsin-Eau Claire, Department of Chemistry, 105 Garfield Avenue, Eau Claire, Wisconsin 54702, and University of Wisconsin-Madison, Department of Chemistry, 1101 W. University Avenue, Madison, Wisconsin 53706

Received May 24, 2004; Revised Manuscript Received November 10, 2004; E-mail: halfenja@uwec.edu; brunold@chem.wisc.edu

Abstract: A combined synthetic/spectroscopic/computational approach has been employed to prepare and characterize a series of Fe(II)−thiolate complexes that model the square-pyramidal [Fe(II)$(N_{His})_4(S_{Cys})$] structure of the reduced active site of superoxide reductases (SORs), a class of enzymes that detoxify superoxide in air-sensitive organisms. The high-spin ($S = 2$) Fe(II) complexes [(Me_4cyclam)Fe(SC_6H_4-*p*-OMe)]OTf (**2**) and [FeL]PF_6 (**3**) (where Me_4cyclam = 1,4,8,11-tetramethylcyclam and L is the pentadentate monoanion of 1-thioethyl-4,8,11-trimethylcyclam) were synthesized and subjected to structural, magnetic, and electrochemical characterization. X-ray crystallographic studies confirm that **2** and **3** possess an N_4S donor set similar to that found for the SOR active site and reveal molecular geometries intermediate between square pyramidal and trigonal bipyramidal for both complexes. Electronic absorption, magnetic circular dichroism (MCD), and variable-temperature variable-field MCD (VTVH-MCD) spectroscopies were utilized, in conjunction with density functional theory (DFT) and semiemperical INDO/S-CI calculations, to probe the ground and excited states of complexes **2** and **3**, as well as the previously reported Fe(II) SOR model [(L^8py_2)Fe(SC_6H_4-*p*-Me)]BF_4 (**1**) (where L^8py_2 is a tetradentate pyridyl-appended diazacyclooctane macrocycle). These studies allow for a detailed interpretation of the S→Fe(II) charge transfer transitions observed in the absorption and MCD spectra of complexes **1**−**3** and provide significant insights into the nature of Fe(II)−S bonding in complexes with axial thiolate ligation. Of the three models investigated, complex **3** exhibits an absorption spectrum that is particularly similar to the one reported for the reduced SOR enzyme (SOR_{red}), suggesting that this model accurately mimics key elements of the electronic structure of the enzyme active site; namely, highly covalent Fe−S π- *and* σ-interactions. These spectral similarities are shown to arise from the fact that **3** contains an alkyl thiolate tethered to the equatorial cyclam ring, resulting in a thiolate orientation that is very similar to the one adopted by the Cys residue in the SOR_{red} active site. Possible implications of our results with respect to the electronic structure and reactivity of SOR_{red} are discussed.

Introduction

In a wide variety of organisms, the detoxification of superoxide ($O_2^{\bullet-}$) is accomplished via its dismutation to hydrogen peroxide (H_2O_2) and molecular oxygen (O_2).[1] In anaerobic bacteria and archaea, though, an alternative strategy has been found that involves only the one-electron reduction of superoxide to H_2O_2, a reaction that is catalyzed by a class of nonheme iron enzymes known as superoxide reductases (SORs).[2,3] Structural studies have revealed that, in all SORs, the active site consists of a mononuclear Fe center ligated by four equatorial histidines and an axial cysteine in a square-pyramidal geometry.[4−6] In the ferric ($S = {}^5/_2$) form of the enzyme (SOR_{ox}), the coordination site trans to the thiolate is occupied by a glutamate residue that dissociates upon conversion to the ferrous ($S = 2$) state (SOR_{red}).[4] Based on the ability of small molecules (N_3^-, CN^-, NO) to coordinate to the Fe center in SOR,[6,7] the reaction with superoxide is believed to proceed by an inner-sphere mechanism. Furthermore, putative Fe(III)−(hydro)peroxo intermediates in the catalytic cycle have been generated in pulse-

[†] University of Wisconsin-Eau Claire.
[‡] University of Wisconsin-Madison.

(1) (a) Valentine, J. S.; Wertz, D. L.; Lyons, T. J.; Liou, L.; Goto, J. J.; Gralla, E. B. *Curr. Opin. Chem. Biol.* **1998**, *2*, 253−262. (b) Fridovich, I. *Annu. Rev. Biochem.* **1995**, *64*, 97−112. (c) Miller, A. F. *Comments Mol. Cell. Biophys.* **1997**, *9*, 1−48.
(2) Jenney, F. E., Jr.; Verhagen, M. F. J. M.; Cui, X.; Adams, M. W. W. *Science* **1999**, *286*, 306−309.
(3) Jovanovic, T.; Ascenso, C.; Hazlett, K. R. O.; Sikkink, R.; Krebs, C.; Litwiller, R.; Benson, L. M.; Moura, I.; Moura, J. J. G.; Radolf, J. D.; Huynh, B. H.; Naylor, S.; Rusnak, F. *J. Biol. Chem.* **2000**, *275*, 28439−28448.
(4) Yeh, A. P.; Hu, Y.; Jenney, F. E., Jr.; Adams, M. W. W.; Rees, D. C. *Biochemistry* **2000**, *39*, 2499−2508.
(5) Coelho, A. V.; Matias, P.; Fulop, V.; Thompson, A.; Gonzalez, A.; Coronado, M. A. *J. Biol. Inorg. Chem.* **1997**, *2*, 680−689.
(6) Clay, M. D.; Jenney, F. E., Jr.; Hagedoorn, P. L.; George, G. N.; Adams, M. W. W.; Johnson, M. K. *J. Am. Chem. Soc.* **2002**, *124*, 788−805.
(7) Clay, M. D.; Cosper, C. A.; Jenney, F. E., Jr.; Adams, M. W. W.; Johnson, M. K. *Proc. Natl. Acad. Sci. U.S.A.* **2003**, *100*, 3796−3801.

radiolysis[8−10] and mutagenesis experiments[11] and studied with spectroscopic and computational[12] methods. Although not confirmed experimentally, it seems likely that the substrate binds to the Fe(II) center in the vacant position trans to the axial cysteine ligand.

The axial cysteine residue in the SOR active site is thought to play a major role in facilitating superoxide reduction and product release, primarily through charge donation to the Fe center. Specifically, spectroscopic studies by Johnson and co-workers have revealed the presence of a strong Fe−S π-bonding interaction between one of the S_{Cys}-based lone pairs and an Fe(d_π) orbital, which is particularly evident from the intense, low-energy $S_{Cys}\rightarrow$Fe(III) charge transfer (CT) transition at 15 150 cm^{-1} in the electronic absorption spectrum of oxidized *P. furiosus* SOR.[6,13] The corresponding transition in the reduced state is found at 31 200 cm^{-1}.[6] It has been suggested that this covalent Fe−S π-interaction facilitates electron transfer to the singly occupied π^* acceptor orbital of superoxide and then promotes dissociation of product peroxide via a trans influence and/or effect.[14] The role of the conserved active-site glutamate residue is less clear. It was initially proposed that the existence of a six-coordinate ferric center prevents superoxide binding to the oxidized enzyme, thus avoiding the possibility of superoxide dismutation that would be detrimental for the organism.[4] Yet further studies have found no significant superoxide oxidation activity upon substitution of this glutamate residue, and the rates of superoxide reduction displayed by the variants were virtually unchanged.[8,9] Alternatively, mutation of a conserved second-sphere lysine residue resulted in a large (20−30-fold) reduction of SOR activity, and it is believed that this residue functions in proton donation to the nascent peroxo intermediate.[9]

The emergence of this novel superoxide detoxification pathway has stimulated the synthesis of structural and functional models of the SOR active site.[15] Kovacs and co-workers have prepared a five-coordinate Fe(II) model with a N_4S ligand set that reacts with superoxide to yield H_2O_2.[16] When the reaction is performed at low temperature (−90 °C), they observe a six-coordinate [Fe(III)(η^1-OOH)] intermediate with a low-spin ($S = {}^1/_2$) ferric center,[17] in which the hydroperoxo ligand is likely trans to one of the N-donor ligands rather than to the thiolate as in the putative protein intermediate. In a previous study, we presented the synthesis of a series of square-pyramidal Fe(II)−thiolate models that feature a vacant coordination site trans to the axial thiolate ligand.[18] This first generation of SOR_{red} model complexes is represented in Scheme 1 by complex **1**,

Scheme 1

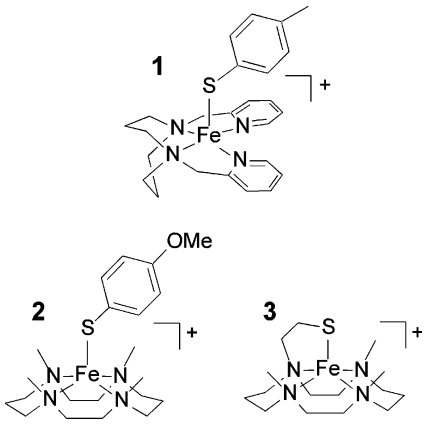

which contains an Fe(II) center supported by the tetradentate ligand 1,5-bis(2-pyridylmethyl)-1,5-diazacyclooctane (L^8py_2) in its equatorial plane and an axial *p*-toluenethiolate ligand. In an effort to expand the range of structural and electronic properties exhibited by SOR_{red} models, we have prepared complexes **2** and **3** (Scheme 1), which are based on the macrocyclic N_4-donor 1,4,8,11-tetraazacyclotetradecane (cyclam). The synthesis and structural characterization of these second- and third-generation SOR_{red} models (**2** and **3**, respectively) is described herein.

Despite the success in generating structural and functional models of the SOR active site, there exist very few studies that have examined in detail the electronic properties of mononuclear Fe(II) complexes with mixed N/S ligation, such as **1**−**3**. Given the importance ascribed to axial thiolate ligation with respect to SOR catalysis, these complexes provide ideal systems through which to explore the effects of structural variations on Fe(II)−thiolate bonding. Therefore, we have engaged in a detailed investigation of models **1**−**3** using a combination of spectroscopic and computational methods. The electronic absorption spectra of these models are dominated by S→Fe(II) CT transitions in the visible and near-UV regions that also produce the major contributions to the corresponding magnetic circular dichroism (MCD) spectra. To estimate the zero-field splitting (ZFS) parameters for these complexes, both a quantitative analysis of variable-temperature variable-field MCD (VTVH-MCD) data and semiemperical INDO/S-CI calculations were performed. Density functional theory (DFT) calculations were used to provide quantitative bonding descriptions of the Fe(II)−thiolate complexes that were validated on the basis of our spectroscopic data. Among other findings, these experimentally calibrated electronic structure descriptions establish an interesting relationship between structural constraints and Fe(II)−S bonding. The implications of these results with respect to the current understanding of Fe(II)−ligand interactions in the SOR_{red} active site are also explored.

Experimental and Computational Procedures

Materials and Methods. All reagents, including the macrocyclic ligand Me_4cyclam, were obtained from commercial sources. [Fe(MeCN)$_2$(OTf)$_2$] was prepared by the reaction of anhydrous $FeCl_2$ with a stoichiometric quantity of triflic acid in anhydrous MeCN, followed by precipitation with anhydrous diethyl ether.[19] Solvents were purified

(8) Coulter, E. D.; Emerson, J. P.; Kurtz, D. M., Jr.; Cabelli, D. E. *J. Am. Chem. Soc.* **2000**, *122*, 11555−11556.
(9) Lombard, M.; Houee-Levin, C.; Touati, D.; Fontecave, M.; Niviere, V. *Biochemistry* **2001**, *40*, 5032−5040.
(10) (a) Abreu, I. A.; Saraiva, L. M.; Soares, C. M.; Teixeira, M.; Cabelli, D. E. *J. Biol. Chem.* **2002**, *276*, 38995−39001. (b) Niviere, V.; Lombard, M.; Fontecave, M.; Houee-Levin, C. *FEBS Lett.* **2001**, *497*, 171−173.
(11) Mathe, C.; Mattioli, T. A.; Horner, O.; Lombard, M.; Latour, J.-M.; Fontecave, M.; Niviere, V. *J. Am. Chem. Soc.* **2002**, *124*, 4966−4967.
(12) Silaghi-Dumitrescu, R.; Silaghi-Dumitrescu, I.; Coulter, E. D.; Kurtz, D. M., Jr. *Inorg. Chem.* **2003**, *42*, 446−456.
(13) Clay, M. D.; Jenney, F. E., Jr.; Noh, H. J.; Hagedoorn, P. L.; Adams, M. W. W.; Johnson, M. K. *Biochemistry* **2002**, *41*, 9833−9841.
(14) Adams, M. W. W.; Jenney, F. E., Jr.; Clay, M. D.; Johnson, M. K. *J. Biol. Inorg. Chem.* **2002**, *7*, 647−652.
(15) Kovacs, J. A. *Chem. Rev.* **2004**, *104*, 825−848.
(16) Shearer, J.; Nehring, J.; Lovell, S.; Kaminsky, W.; Kovacs, J. A. *Inorg. Chem.* **2001**, *40*, 5483−5484.
(17) Shearer, J.; Scarrow, R. C.; Kovacs, J. A. *J. Am. Chem. Soc.* **2002**, *124*, 11709−11717.
(18) Halfen, J. A.; Moore, H. L.; Fox, D. C. *Inorg. Chem.* **2002**, *41*, 3935−3943.
(19) Dixon, N. E.; Lawrance, G. A.; Lay, P. A.; Sargeson, A. M.; Taube, H. *Inorg. Synth.* **1990**, *28*, 70−76.

according to standard methods. All reactions were conducted, and products were handled, under an inert atmosphere using a Vacuum Atmospheres glovebox. Electrochemical experiments were conducted with a BAS Epsilon potentiostat, using a platinum disk working electrode, a silver wire pseudo-reference electrode, and a platinum wire auxiliary electrode. Cyclic voltammograms were obtained in MeCN (0.1 M *n*-Bu_4NClO_4) with an analyte concentration of 1 mM. Ferrocene was used as an internal standard, and its redox potential under the experimental conditions was adjusted to the literature value (+380 mV vs SCE).[20] Other analyte redox potentials were shifted accordingly. Solid-state magnetic susceptibilities were determined at room temperature using a Johnson−Matthey magnetic susceptibility balance. Elemental analyses were performed by Atlantic Microlabs (Norcross, GA).

[(Me$_4$cyclam)Fe(SC$_6$H$_4$-*p*-OMe)]OTf (2): A solution of Me_4cyclam (51 mg, 0.199 mmol) dissolved in THF (5 mL) was treated with [Fe(MeCN)$_2$(OTf)$_2$] (84 mg, 0.193 mmol). After stirring for 20 min, solid $NaSC_6H_4$-*p*-OMe (34 mg, 0.210 mmol) was added to the solution, resulting in the development of a light yellow color. After 2 h, the solvent was removed from the mixture under vacuum, and the solid residue was extracted into CH_2Cl_2 (5 mL) and then filtered through a glass wool plug. Addition of Et_2O to the filtrate provided the crude product as an off-white solid, which was recrystallized from CH_2Cl_2/Et_2O to afford pure **2** as very light pink prisms, 55 mg (47%). Anal. Calcd for $C_{22}H_{39}F_3FeN_4O_4S_2$: C, 44.00; H, 6.54; N, 9.33. Found: C, 44.01; H, 6.46; N, 9.27.

[LFe]PF$_6$ (3): A solution of 1-thioethyl-4,8,11-trimethylcyclam (127 mg, 0.420 mmol)[21] in MeOH (5 mL) was treated with LiOH·H_2O (17.5 mg, 0.417 mmol). Solid [Fe(MeCN)$_2$(OTf)$_2$] (182 mg, 0.418 mmol) was added after stirring for 30 min, and stirring continued for an additional 30 min. The cloudy mixture was then filtered through a Celite pad, and a solution of NH_4PF_6 (215 mg, 1.32 mmol) in MeOH (3 mL) was added, resulting in the deposition of a crystalline solid. The mixture was filtered, and the solid was redissolved in a mixture of CH_2Cl_2 and MeCN (2:1, 10 mL). This solution was filtered through a Celite pad, and the filtrate was treated with excess diethyl ether to produce **3** as a colorless crystalline solid, 125 mg (60%). Anal. Calcd for $C_{15}H_{33}F_6FeN_4PS\cdot 0.25CH_2Cl_2$: C, 34.98; H, 6.45; N, 10.70. Found: C, 35.08; H, 6.45; N, 10.79. The presence of fractional solvent in the crystal lattice of **3** was confirmed by X-ray crystallography.

X-ray Crystallography. Single crystals were mounted in thin-walled glass capillaries and transferred to a Bruker-Nonius MACH3S X-ray diffractometer for data collections at −150(2) °C (**2**) or −100(2) °C (**3**) using graphite monochromated Mo Kα ($\lambda = 0.710\ 73$ Å) radiation. Unit cell constants were determined from a least-squares refinement of the setting angles of 25 intense, high angle reflections. Intensity data were collected using the $\omega/2\theta$ scan technique to a maximum 2θ value of 53.94° (**2**) or 49.94° (**3**). The data were corrected for Lorentz and polarization effects and converted to structure factors using the teXsan for Windows crystallographic software package.[22a] Space groups were determined based on systematic absences and intensity statistics. Successful direct-method solutions were calculated for each compound using the SHELXTL suite of programs.[22b] Non-hydrogen atoms that were not identified from the initial E-map were located after several cycles of structure expansion and full matrix least squares refinement on F^2. Hydrogen atoms were added geometrically. All non-hydrogen atoms were refined with anisotropic displacement parameters, while hydrogen atoms were refined using a riding model with group isotropic displacement parameters. Relevant crystallographic results for **2** and **3** are summarized in Tables S1 and S2. Complete crystallographic data for each compound in CIF format are provided as Supporting Information.

The asymmetric unit of **2** includes two crystallographically independent formula units. One of the two $CF_3SO_3^-$ ions is rotationally disordered about the C−S bond; a split-atom model featuring two independent conformations for the anion, with refined occupancies of 0.597(7) and 0.403(7), was used to account for the disorder. Bond length and angle constraints were applied to the disordered anion. The absolute structure of the sample was assigned by consideration of the Flack *x* parameter, in this case 0.00(2). The X-ray crystal structure of **3** contains a disordered cation, two partially occupied yet ordered anion positions, and a disordered, half-occupied CH_2Cl_2 solvate that resides on a special position possessing $\bar{3}$ site symmetry. The Fe center in **3** resides on a crystallographic 2-fold axis, necessitating 2-fold rotational disorder for the cation. In addition, there is pseudo-mirror disorder within the cation, resulting in each alkyl spacer between adjacent nitrogen donors appearing as a statistical combination of ethylene ($-C_2H_4-$) and propylene ($-C_3H_6-$) groups. Bond length and angle constraints were applied to all of the disordered alkyl groups. Analysis of the final refined structure using the PLATON suite of programs[23] revealed a potential alternative space group assignment ($P6_3/mcm$). However, the structure of **3** could not be solved in this alternative space group, and an attempt to transform the structure that was solved and refined in $P\bar{3}c1$ into $P6_3/mcm$ resulted in an unstable refinement. Thus, we conclude that the appropriate space group for **3** is $P\bar{3}c1$, and that the alternative space group identified by PLATON is disallowed by the substantial cation disorder. Attempts to disrupt the cation disorder in **3** by anion metathesis (ClO_4^-, $CF_3SO_3^-$, BPh_4^-) resulted in either more significant disorder or in poorly diffracting samples. No attempts were made to locate or calculate the positions of the hydrogen atoms of the half-occupied, disordered CH_2Cl_2 solvate. These atoms are omitted from the empirical formula and the calculations of F_{000} and d_{calcd} for **3**.

Absorption and MCD Spectroscopies. Room-temperature electronic absorption spectra of **1**−**3** were measured using a Hewlett-Packard 8453 spectrophotometer. Variable temperature absorption and MCD spectra were recorded using a Jasco J-715 spectropolarimeter in conjunction with an Oxford Instruments SM-4000 8T magnetocryostat. The solid-state samples of **1**−**3** used for low-temperature absorption and MCD studies were prepared as uniform mulls in poly(dimethylsiloxane) (Aldrich). Frozen solution samples were prepared by dissolving the complexes in a 2:1 mixture of MeOH and glycerol.

VTVH-MCD data were analyzed using the software program developed by Dr. Frank Neese (MPI Mülheim an der Ruhr, Germany).[24] To locate the best overall fit for each model **1**−**3**, the *D* and *E*/*D* values were systematically varied over the ranges of $-20\ cm^{-1} < D < 20\ cm^{-1}$ and $0 < E/D < 0.33$. The *g*-values used in the fitting routine were obtained from INDO/S-CI calculations performed on **1**−**3** (vide infra).[25] For each set of ZFS parameters the three transition moment products (M_{xy}, M_{xz}, and M_{yz}) were adjusted to achieve the best agreement between the experimental and calculated VTVH-MCD data, as quantified by the goodness-of-fit parameter (χ^2):

$$\chi^2 = \sum_{i=1}^{N} (I_i^{(calcd)} - I_i^{(expt)})^2$$

Computational Methods. (a) Computational Models. For complex **1**, the computational model used in DFT and INDO/S-CI calculations was based completely on the X-ray crystal structure[18] and included the entire complex except for the counteranion. To obtain a computational model of complex **2**, the coordinates of the first-sphere atoms (consisting of the $FeSN_4$ core, along with C_1 of the aryl ring) of the two structurally distinct cations in the X-ray structure were averaged to produce a composite structure, and the positions of all remaining atoms in the cyclam and aryl rings were geometry-optimized. Similarly,

(20) Connelly, N. G.; Geiger, W. E. *Chem. Rev.* **1996**, *96*, 877−910.
(21) Halfen, J. A.; Young, V. G., Jr. *Chem. Commun.* **2003**, 2894−2895.
(22) (a) *TeXsan for Windows V 1.02*; Molecular Structure Corporation, Inc.: The Woodlands, TX. (b) *SHELXTL V. 5.1 for Windows NT*; Bruker AXS: Madison, WI.
(23) Spek, A. L. *J. Appl. Crystallogr.* **2003**, *36*, 7−13.
(24) (a) Neese, F.; Solomon, E. I. *Inorg. Chem.* **1998**, *37*, 6568−6582. (b) Neese, F.; Solomon, E. I. *Inorg. Chem.* **1999**, *38*, 1847−1865.

the crystallographic disorder in the positions of the cyclam ring atoms of complex **3** required optimization of all atoms beyond the first sphere. All geometry optimizations were performed with the Amsterdam Density Functional (ADF) 2002.03 software package[26] on a cluster of 20 Intel Xeon processors (Ace computers) using ADF basis set IV (triple-ζ with single polarization on the ligand atoms), an integration constant of 4.0, and the Vosko−Wilk−Nusair[27] local density approximation with the nonlocal gradient corrections of Becke[28] and Perdew.[29] The Cartesian coordinates for the DFT geometry-optimized models of **2** and **3** are provided in Tables S3 and S4 (see ref 18 for structural parameters of **1**).

(b) DFT Calculations. All single-point DFT calculations were performed using the ORCA 2.2 software package developed by Neese.[30] Computations on models **1**−**3** were carried out using a spin unrestricted formalism, while those on the free ligands were performed spin restricted. For the first-sphere atoms (Fe, N, S), Ahlrichs' valence triple-ζ basis set[31] with one (N) or two (Fe, S) sets of polarization functions[32] were used. The remaining atoms utilized Ahlrich's split valence basis set[31] with one set of polarization functions on all nonhydrogen atoms, along with the corresponding auxiliary basis set (SV/J).[33] The calculations were performed with the local density approximation of Perdew and Wang[34] and the nonlocal corrections of Becke[28] and Perdew,[29] using an integration grid of 4.0. The gOpenMol program developed by Laaksonen[35] was used to generate boundary surface plots of molecular orbitals (using an isodensity value of 0.05 b^{-3}).

(c) Semiemperical INDO/S-CI Calculations. Semiemperical calculations employing the INDO/S model developed by Zerner and coworkers[36] were also performed using the ORCA program.[30] The calculations used the valence-shell ionization potentials and Slater−Condon parameters listed by Bacon and Zerner,[37] the standard interaction factors $f_{p\sigma p\sigma} = 1.266$ and $f_{p\pi p\pi} = 0.585$, and the following spin−orbit coupling constants: $\zeta_{3d}(Fe) = 400\ cm^{-1}$, $\zeta_{4p}(Fe) = 445\ cm^{-1}$, $\zeta_{3p}(S) = 250\ cm^{-1}$, $\zeta_{2p}(N) = 76\ cm^{-1}$, and $\zeta_{2p}(O) = 150\ cm^{-1}$. Restricted open-shell Hartree−Fock (ROHF) SCF calculations were converged onto the spin quintet ground states of models **1**−**3**, which served as the reference states for configuration interaction (CI) calculations. Descriptions of the active spaces used for all INDO/S-CI calculations of **1**−**3** are provided in the Supporting Information.

Results and Analysis

Complex Design and Syntheses. Our first generation of SOR_{red} model complexes is represented by complex **1** (Scheme 1), the synthesis of which was described earlier.[18] While complex **1** contains a square-pyramidal Fe(II) center supported by the tetradentate ligand L^8py_2 in its equatorial plane and an axial *p*-toluenethiolate ligand, complexes **2** and **3** (Scheme 1) utilize the macrocyclic N_4-donor 1,4,8,11-tetraazacyclotetradecane (cyclam). The coordination sphere of **2** includes the tetra-*N*-methylated macrocycle Me_4cyclam and is completed by a 4-methoxybenzenethiolate ligand, whereas complex **3** is coordinated by a single pentadentate ligand, derived from cyclam, which features a pendant thioethyl group.[21]

Scheme 2

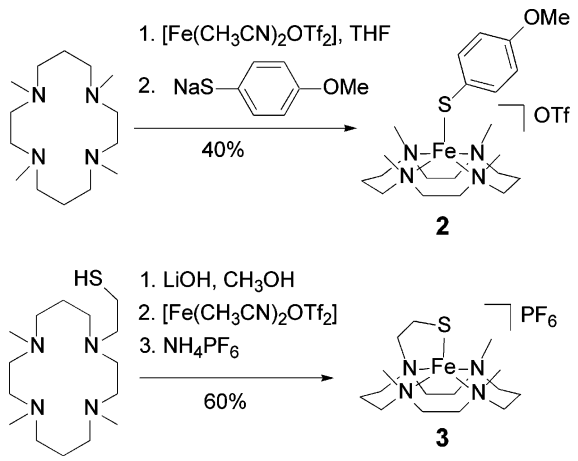

A convenient one-pot synthesis was used to prepare complex **2**, a methodology that is equally applicable to related complexes containing other aryl- or alkylthiolate ligands (Scheme 2). Specifically, equimolar amounts of Me_4cyclam and $[Fe(MeCN)_2(OTf)_2]$ were combined in THF, generating $[(Me_4cyclam)Fe(OTf)]OTf$ in situ.[38] Addition of sodium 4-methoxybenzenethiolate, followed by recrystallization of the crude product from CH_2Cl_2, afforded the SOR_{red} model complex **2** as a colorless crystalline solid in moderate yield (47%).[39] The synthesis of **3**, which possesses a thioethyl-pendant trimethylcyclam ligand, was achieved following a different strategy. The pentadentate ligand suffers from facile aerobic degradation, and as a result, small quantities of the ligand were prepared by the reaction of trimethylcyclam with thirane immediately prior to metalation. Deprotonation of the thiol-pendant ligand with LiOH in MeOH, followed by metalation with $[Fe(MeCN)_2(OTf)_2]$ and anion metathesis with NH_4PF_6, afforded complex **3** as a colorless solid in yields approaching 60% (Scheme 2). Interestingly, **3** could be isolated in reasonable yield only when prepared in a protic solvent (MeOH); attempts to prepare **3** under anhydrous conditions (deprotonation using NaH followed by metalation in THF) led to substantially reduced yields of product. Apparently, the basic nature of the reaction medium is sufficient to allow metalation, rather than protonation, of the pentadentate ligand.

Structural, Magnetic, and Electrochemical Characterization. The solid-state structures of **2** and **3** were determined by X-ray crystallography. A summary of the crystallographic results is presented in Table S1, and significant interatomic distances

(25) In all cases, the *g*-values were in the range 2.01−2.08, and variations in these values had only negligible effects on the quality of the resulting fits. Specifically, our analysis revealed that the overall shapes of the VTVH-MCD magnetization curves are determined principally by the ZFS parameters, not the *g*-values.
(26) (a) Baerends, E. J.; Ellis, D. E.; Ros, P. *Chem. Phys.* **1973**, *2*, 41. (b) Versluis, L.; Ziegler, T. *J. Chem. Phys.* **1988**, *88*, 322−328. (c) te Velde, G.; Baerends, E. J. *J. Comput. Phys.* **1992**, *99*, 84−98. (d) Guerra, C. F.; Snijders, J. G.; te Velde, G.; Baerends, E. J. *Theor. Chem. Acc.* **1998**, *99*, 391−403.
(27) Vosko, S. H.; Wilk, L.; Nusair, M. *Can. J. Phys.* **1980**, *58*, 1200−1211.
(28) Becke, A. D. *J. Chem. Phys.* **1986**, *84*, 4524−4529.
(29) Perdew, J. P. *Phys. Rev. B: Condens. Matter* **1986**, *33*, 8822−8824.
(30) Neese, F. *ORCA*, version 2.2.; an ab initio, density functional, and semiempirical program package; Max-Plack Institut für Bioanorganische Chemie: Mülheim an der Ruhr, Germany, 2001.
(31) Schaefer, A.; Horn, H.; Ahlrichs, R. *J. Chem. Phys.* **1992**, *97*, 2571.
(32) Ahlrichs, R. Unpublished results.
(33) (a) Eichkorn, K.; Treutler, O.; Ohm, H.; Haser, M.; Ahlrichs, R. *Chem. Phys. Lett.* **1995**, *240*, 283. (b) Eichkorn, K.; Weigend, F.; Treutler, O.; Ahlrichs, R. *Theor. Chem. Acc.* **1997**, *97*, 119.
(34) Perdew, J. P.; Wang, Y. *Phys. Rev. B: Condens. Matter* **1992**, *45*, 13244−13249.
(35) (a) Laaksonen, L. *J. Mol. Graphics* **1992**, *10*, 33. (b) Bergman, D. L.; Laaksonen, L.; Laaksonen, A. *J. Mol. Graphics Modell.* **1997**, *15*, 301.
(36) (a) Ridley, J.; Zerner, M. C. *Theor. Chem. Acc.* **1973**, *32*, 111. (b) Zerner, M. C.; Loew, G. H.; Kirchner, R. F.; Mueller-Westerhof, U. T. *J. Am. Chem. Soc.* **1980**, *102*, 589.
(37) Bacon, A. D.; Zerner, M. C. *Theor. Chem. Acc.* **1979**, *53*, 21.
(38) Rohde, J.-U.; In, J. H.; Lim, M. H.; Brennessel, W. W.; Bukowski, M. R.; Stubna, A.; Munck, E.; Nam, W.; Que, L., Jr. *Science* **2003**, *299*, 1037−1039.
(39) The use of hydrated Fe(II) sources or protic solvents during the metalation of Me_4cyclam led to very low yields of the final Fe(II)−thiolate complexes, presumably due to protonation of the macrocyclic ligand. This synthetic difficulty was not encountered during the preparation of **1** or related SOR_{red} models supported by L^8py_2, which reflects the enhanced proton affinity of Me_4cyclam over the pyridyl-pendant diazacyclooctane ligand.

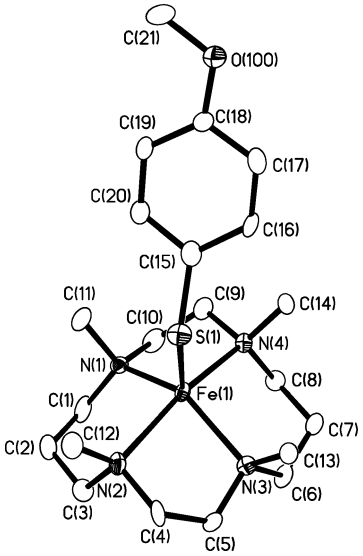

Figure 1. Thermal ellipsoid representation (50% probability boundaries) of one of the two crystallographically independent cations in the X-ray crystal structure of **2**, with hydrogen atoms omitted for clarity. Significant interatomic distances (Å) and angles (°) include the following: Fe1−N1, 2.183(6); Fe1−N2, 2.279(6); Fe1−N3, 2.186(5); Fe1−N4, 2.237(5); Fe1−S1, 2.3220(18); N1−Fe1−N2, 90.9(2); N1−Fe1−N3, 136.7(2); N1−Fe1−N4, 84.4(2); N2−Fe1−N3, 81.4(2); N2−Fe1−N4, 164.1(2); N3−Fe1−N4, 91.6(2); S1−Fe1−N1, 113.33(15); S1−Fe1−N2, 92.30(15); S1−Fe1−N3, 109.58(15); S1−Fe1−N4, 103.53(15); Fe1−S1−C15, 125.3(2).

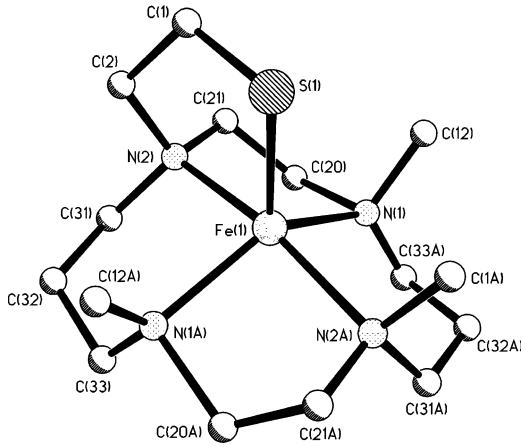

Figure 2. Ball and stick representation of the cationic portion of the X-ray crystal structure of **3** with hydrogen atoms omitted for clarity. Significant interatomic distances (Å) and angles (°) include the following: Fe1−N1, 2.176(5); Fe1−N2, 2.225(5); Fe1−S1, 2.297(3); N1−Fe1−N2, 87.4(2); N1−Fe1−N1A, 137.6(3); N1−Fe1−N2A, 88.0(2); N2−Fe1−N2A, 167.2(3); N1A-Fe1−N2A, 87.4(2), S1−Fe1−N1, 111.2(4); S1−Fe1−N2, 89.5(2); S1−Fe1−N1A, 110.8(4); S1−Fe1−N2A, 103.3(2); Fe1−S1−C1, 98.0(5).

and angles are presented in the captions of Figures 1 and 2. Full details of the structure determinations (in CIF format) are provided as Supporting Information.

The asymmetric unit of **2** contains two compositionally identical formula units that exhibit some slight metrical differences; a thermal ellipsoid representation of one of the two independent Fe(II)−thiolate cations in **2** is shown in Figure 1. Each of the two cations contains a pentacoordinate Fe(II) ion ligated by the Me_4cyclam macrocycle and a single thiolate ligand. In each case, the macrocycle is found in the *trans-I* conformation, with the thiolate ligand and the four *N*-methyl groups occupying the same face of the complex. Both cations exhibit significant distortions from an idealized square-pyramidal geometry, as indicated by the shape-defining parameter τ (0.57 and 0.46 for the two crystallographically independent cations).[40,41] The distortions of these Fe(II)−thiolate cations toward a more trigonal-bipyramidal geometry gives rise to asymmetry in their Fe−N bond lengths, such that the Fe−N bonds in the pseudo-trigonal planes (including the sulfur donors) are shorter than the "axial" Fe−N bonds. Differences in the metrical parameters between the two independent cations illustrate the structural flexibility provided by the Me_4cyclam macrocycle. While differences in bond lengths between pairs of equivalent Fe-ligand bonds in the two cations are generally small (0.01−0.03 Å), some equivalent N−Fe−N bond angles vary by as much as 6°, and bond angles involving the sulfur donor differ by as much as 10°.

As described in the Experimental Section, substantial 2-fold rotational and pseudo-mirror disorder in the Fe(II) cation of **3** precludes a detailed analysis of the structural properties of this complex. However, a cursory examination of the structure of **3** reveals some of the same structural features identified in the X-ray crystal structure of **2**. Specifically, the Fe(II) center in **3** adopts a distorted pentacoordinate geometry ($\tau = 0.50$)[41] with the pendant thioalkyl arm residing on the same face of the macrocycle as the three *N*-methyl groups (Figure 2). The macrocyclic ligand is again found in the *trans*-I conformation, and the asymmetry in the Fe−N bond lengths identified in **2** persists in **3**. While the Fe−S bond length in **3** is similar to that in **2**, the constrained nature of the five-membered chelate ring that includes the thiolate donor causes the Fe−S−C bond angle in **3** to be significantly more acute than that in **2**: 98.0(5)° in **3** vs 115.9(2)° and 125.3(2)° for the two independent cations in **2**.

Similar to **1**, both **2** and **3** contain high-spin Fe(II) centers as suggested by their Fe−N bond lengths[42] and verified by room-temperature magnetic susceptibility measurements (**2**, $\mu_{eff} = 4.9\ \beta$; **3**, $\mu_{eff} = 5.1\ \beta$). The high-spin, $S = 2$ ground states of these Fe(II) complexes parallel that of the SOR_{red} active site.[3,6] Complex **1** was previously shown to undergo irreversible oxidation at a potential (+615 mV vs SCE) that renders it inert toward aerobic oxidation.[18] The overall electrochemical properties of **2** and **3** are similar to those of **1** in that both complexes are irreversibly oxidized, albeit at potentials slightly depressed relative to that of **1** (**2**, +570 mV; **3**, +530 mV vs SCE). The lower redox potentials may be due to the more electron-donating thiolate ligands and/or more basic macrocycles in complexes **2** and **3**, factors that would be expected to aid in the stabilization of the Fe(III) state. However, the oxidized counterparts of **2** and **3** have yet to be isolated as stable materials.

Electronic Absorption Spectroscopy. The room temperature (rt) electronic absorption spectra of complex **1** in MeCN and complexes **2** and **3** in CH_2Cl_2 are shown in Figure 3. Although the bands of **2** are uniformly more intense and ~4000 cm^{-1} higher in energy than those of **1**, the spectra of **1** and **2** bear a close resemblance to each other in terms of their overall

(40) The geometric parameter τ is defined as $\tau = |(\beta - \alpha)|/60$, where α and β are the two trans basal angles in psuedo-square pyramidal geometry (see ref 41). In idealized square-planar geometries, $\alpha = \beta$, but trigonal distortions result in $\alpha \neq \beta$.

(41) Addison, A. W.; Rao, T. N.; Reedijk, J.; van Rijn, J.; Verschoor, G. C. *J. Chem. Soc., Dalton Trans.* **1984**, 1349−1356.

(42) (a) Blakesley, D. W.; Payne, S. C.; Hagen, K. S. *Inorg. Chem.* **2000**, *39*, 1979−1989. (b) Diebold, A.; Hagen, K. S. *Inorg. Chem.* **1998**, *37*, 215−223.

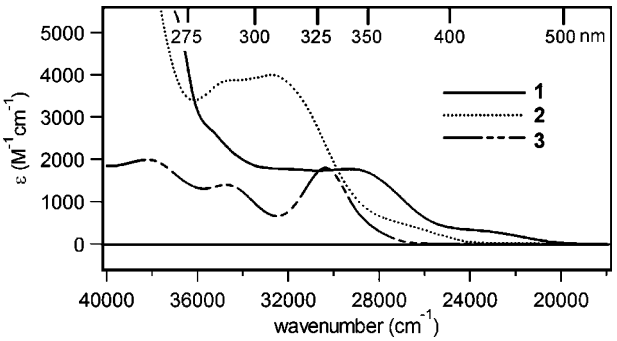

Figure 3. Room-temperature electronic absorption spectra of complex **1** in MeCN solution and of complexes **2** and **3** in CH_2Cl_2 solution.

Table 1. Summary of Electronic Absorption Features for **1**−**3**

complex	solvent[a] (*T*)[b]	λ_{max}, cm^{-1} (ϵ, M^{-1} cm^{-1})[c]
1	MeCN (rt)	29 200 (1800), sh 24 000 (400)
2	CH_2CH_2 (rt)	32 600 (4000), sh ∼28 000 (600)
	MeOH (rt)	34 000 (1700), sh ∼31 500 (900), sh ∼29 000 (200)
	solid state (15 K)	31 100, sh ∼27 000
3	CH_2CH_2 (rt)	38 100 (2000), 34 700 (1400), 30 400 (1800)
	MeOH (rt)	39 500 (2600), 35 900 (1500), 31 200 (1800)
	solid state (15 K)	38 000, 35 000, 30 500, sh 28 900

[a] Solid state = mull in poly(dimethylsiloxane). [b] rt = room temperature. [c] ϵ values are not available for solid-state data.

appearance. Both spectra are comprised of two main features: (i) a low-energy shoulder of weak intensity and (ii) a more intense band to higher energy (Table 1). In contrast, the absorption spectrum of complex **3** is composed of three features of approximately equal intensity centered at 30 400, 34 700, and 38 000 cm^{-1}. As none of these absorption features of **1**−**3** are present in the precursor $Fe(II)N_4$ complexes that lack thiolate ligation, they can be attributed to S→Fe(II) charge transfer (CT) transitions.[43] At energies > 40 000 cm^{-1}, the complexes exhibit intense ligand-based and N→Fe(II) CT transitions.

The absorption spectra of complexes **2** and **3** were also studied in MeOH (Figure S1), a solvent with the potential of coordinating to the Fe(II) center. For **3**, the major features exhibit blue-shifts of 800−1400 cm^{-1} when the CH_2Cl_2 solvent is replaced by MeOH, although the general appearance of the spectrum remains the same (Table 1). For **2**, this change in solvent results in a 1400 cm^{-1} blue-shift of the most intense absorption band and a dramatic overall reduction in band intensities, implying a more significant perturbation of the ligand environment of the Fe(II) center. Based on these results, we conclude that MeOH is coordinating to the Fe(II) centers of both complexes, although the interaction appears to be stronger for complex **2** than for **3**.

To probe the electronic structures of complexes **1**−**3** in the solid state where possible complications due to solvent coordination are avoided, the corresponding 15 K mull absorption spectra were also obtained (Figure S2). While the positions of the low-energy bands remain essentially unchanged for **1**, the most intense absorption feature of **2** now appears at 31 100 cm^{-1}, compared to 32 600 cm^{-1} in CH_2Cl_2 and 34 000 cm^{-1} in MeOH (Table 1). In the solid-state spectrum of complex **3**, the sharpening of the transitions that give rise to the low-energy band reveals the presence of an additional weak feature at 28 900 cm^{-1}, alongside the dominant band at 30 500 cm^{-1}. The two higher-energy bands appear at 35 000 and 38 000 cm^{-1} in the solid state (Table 1).

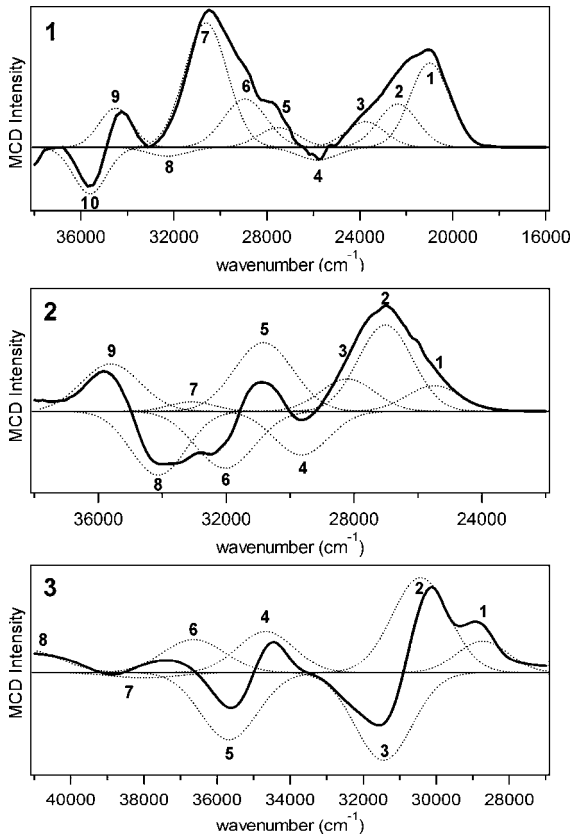

Figure 4. Gaussian-resolved (····) solid-state MCD spectra (—) of complexes **1**−**3**. Spectra were obtained with a magnetic field of 7 T at a temperature of 4 K for **1** and **2** and 20 K for **3**. Band energies and parameters are summarized in Table 2. Note that each spectrum is plotted over a different energy range (*x*-axes are not the same for **1**−**3**).

Solid-State (Mull) MCD Spectroscopy. Figure 4 displays the solid-state (mull) MCD spectra obtained for complexes **1**−**3**. All band intensities increase with decreasing temperature (data not shown), consistent with the expected ***C***-term behavior of these paramagnetic $S = 2$ spin systems. Simultaneous fitting of the low temperature (LT) absorption and MCD spectra required 8−10 Gaussian bands (dotted lines in Figure 4) of roughly equal bandwidths, with peak positions and intensities as indicated in Table 2 (see Figure S3 for Gaussian fits of the absorption data). The MCD spectrum of **1** is characterized by two broad positive features that coincide with the two dominant CT bands in the absorption spectrum. While the MCD spectrum of **2** also exhibits a positively signed low-energy feature, the high-energy region instead contains large contributions from negatively signed transitions.[45] The transitions that give rise to the most intense peak in the LT absorption spectrum of **2** appear

(43) The ligand field (LF) transitions of high-spin Fe(II) complexes, which typically appear in the NIR region, are very weak in both absorption and MCD spectra.[44] Consequently, our absorption and solid-state MCD studies of **1**−**3** failed to detect any such transitions. In constrast, MCD spectra obtained with a concentrated (10 mM) solution of **1** in 1:1 propionitrile/butyronitrile solvent did reveal a LF band at ∼15 000 cm^{-1} (data not shown).

(44) (a) Pavel, E. G.; Kitajima, N.; Solomon, E. I. *J. Am. Chem. Soc.* **1998**, *120*, 3949−3962. (b) Solomon, E. I.; Pavel, E. G.; Loeb, K. E.; Campochiaro, C. *Coord. Chem. Rev.* **1995**, *144*, 369−460.

(45) Although the solid-state sample of **2** contains two crystallographically distinct complexes (cations I and II), the structural differences are too small to cause the appearance of two sets of bands that can be resolved in the MCD spectrum but may possibly lead to a general broadening of the bands.

Table 2. Fit Parameters from Gaussian Deconvolutions of the Experimental Absorption and MCD Spectra of Complexes **1**−**3**

Complex **1**

band	energy (cm^{-1})	ϵ^a ($M^{-1}\,cm^{-1}$)	osc. str. ($f_{exp} \times 10^3$)[b]	rel. MCD intensity[c]
1	21 000	290	2.7	70
2	22 400	300	2.8	35
3	23 750	270	2.5	21
4	25 850	480	4.4	−10
5	27 500	850	7.2	15
6	28 950	1270	12.7	41
7	30 600	970	9.7	100
8	32 250	800	8.0	−7
9	34 500	470	4.7	32
10	35 600	410	3.8	−38

Complex **2**

band	energy (cm^{-1})	ϵ^a ($M^{-1}cm^{-1}$)	osc. str. ($f_{exp} \times 10^3$)[b]	rel. MCD intensity[c]
1	25 500	390	3.6	30
2	27 000	690	6.4	100
3	28 200	1260	11.6	37
4	29 650	1540	14.2	−50
5	30 850	2270	20.9	79
6	32 050	2470	26.5	−65
7	33 100	1060	8.9	11
8	34 100	2020	18.6	−73
9	35 600	1600	16.0	55

Complex **3**

band	energy (cm^{-1})	ϵ^a ($M^{-1}\,cm^{-1}$)	osc. str. ($f_{exp} \times 10^3$)[b]	rel. MCD intensity[c]
1	28 750	400	3.4	33
2	30 450	1350	11.4	100
3	31 450	740	6.3	−92
4	34 650	960	8.1	43
5	35 700	410	3.5	−71
6	36 650	200	1.8	35
7	38 000	1370	13.6	−5
8	41 250	560	6.0	24

[a] Epsilon values (ϵ) for the low-temperature mull spectra were estimated by comparison to the corresponding rt solution spectra, for which ϵ-values are available. [b] $f_{exp} = (4.61 \times 10^{-9})\epsilon_{max}\nu_{1/2}$. [c] Since $\Delta\epsilon$ values are not available for mull spectra, only relative intensities are reported. The largest peak is scaled to 100.

in the MCD spectrum as a derivative-shaped feature centered at 31 600 cm^{-1}, consisting of two bands (bands 5 and 6) of nearly equal intensity but opposite sign. Such features in MCD spectra are commonly referred to as pseudo-***A*** terms and require that the two transitions involved be differently polarized. In the high-energy region, the MCD spectra of both **1** and **2** exhibit similar pseudo-***A*** terms centered near 35 000 cm^{-1} (bands 9/10 and 8/9, respectively).

The MCD spectrum of **3** reveals three closely spaced bands in the low-energy region: a weak positive feature at 28 750 cm^{-1} (band 1) and an intense pseudo-***A*** term feature centered at 30 900 cm^{-1} (bands 2 and 3). These three transitions combine to produce the intense band at 30 400 cm^{-1} in the corresponding rt absorption spectrum. Similarly, the two transitions that produce the pseudo-***A*** term centered at 35 000 cm^{-1} (bands 4 and 5) are the primary contributors to the second absorption band. Notably, the transition that gives rise to the highest-energy absorption band at 38 000 cm^{-1} (band 7) carries very little intensity in the MCD spectrum of **3**.

VTVH-MCD Data Analysis. For each complex, VTVH-MCD data sets were collected at two wavelengths: 330 nm (30 300 cm^{-1}) and 470 nm (21 300 cm^{-1}) for **1**, 307 nm (32 600 cm^{-1}) and 370 nm (27 000 cm^{-1}) for **2**, and 281 nm (35 600 cm^{-1}) and 314 nm (31 800 cm^{-1}) for **3**. These positions were selected so as to coincide with the dominant CT absorption features exhibited by the three complexes in the solid state. Figure 5 shows the low-energy VTVH-MCD data sets obtained for **1**−**3** at the wavelengths indicated; the corresponding high-energy data sets are shown in Figure S4.

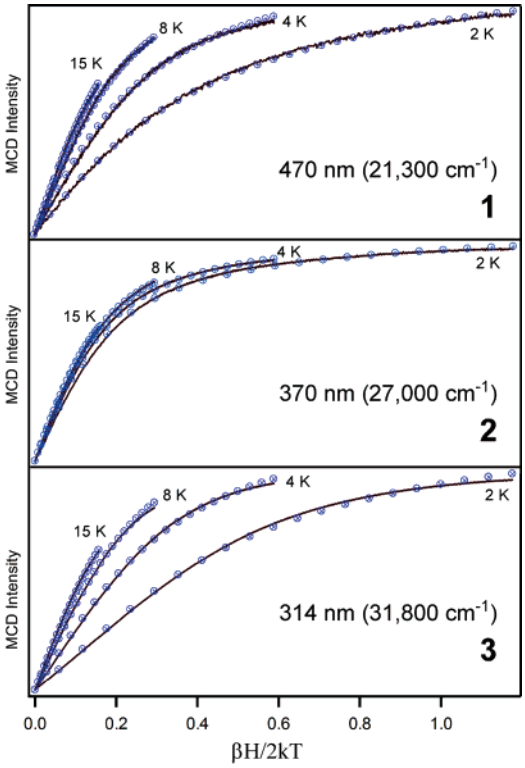

Figure 5. Experimental VTVH-MCD data collected at the indicated wavelengths for complexes **1**−**3** (solid lines), plotted against $\beta H/2kT$. VTVH-MCD experiments were performed by measuring the signal intensity at four different temperatures (2, 4, 8, and 15 K) as a function of magnetic field between 0 and 7 T. Theoretical fits (⊗) were obtained using the "best fit" ZFS values listed in Table 3.

As discussed in seminal papers by Neese and Solomon, the VTVH-MCD saturation behavior of $S > {}^1/_2$ systems depends on the ZFS parameters (D, E/D), the three g-values, and the polarization of the corresponding transition with respect to the molecular coordinate system (as defined by the **D**-tensor).[24] As is evident in Figure 5, the VTVH curves obtained for complexes **1** and **3** are quite similar in terms of general appearance but distinctly different from those obtained for complex **2**, indicating a substantial difference in ZFS parameters and/or transition polarizations. For **1** and **3**, the MCD signal intensity saturates slowly with magnetic field (H), and the curves obtained at different temperatures exhibit a large spread (i.e., the curves are highly "nested"), while the corresponding curves for **2** saturate quickly and display little nesting. By comparison to other Fe(II) complexes, the VTVH-MCD results for **1** and **3** are characteristic of systems with positive ZFS ($D > 0$ cm^{-1}), while those for **2** suggest a negative ZFS ($D < 0$ cm^{-1}).[44] These qualitative conclusions were verified by quantitatively analyzing the VTVH-MCD data within the theoretical framework developed by Neese and Solomon.[24] With this type of analysis it is possible to accurately estimate the ZFS parameters of a given system, as we recently demonstrated in a combined high-field

Table 3. Comparison of Experimental and INDO/S-CI Calculated ZFS Parameters for Complexes **1**−**3**

	experimental ZFS parameters[a]				INDO/S-CI	
complex	probe wavelength (wavenumbers)		D (cm^{-1})	E/D	D (cm^{-1})	E/D
1	470 nm (21 300 cm^{-1})	best fit	+ 9.0	0.20	+3.7	0.24
		range[b]	$D > +4.0$	$0.10 < E/D < 0.25$		
2	370 nm (27 000 cm^{-1})	best fit	−12.0	0.20	−4.7	0.12
		range[b]	$D < -9.0$	$0.15 < E/D < 0.30$		
3	314 nm (31 800 cm^{-1})	best fit	+5.0	0.05	−3.8	0.23
		range[b]	$+4.0 < D < +11.0$	$0.04 < E/D < 0.15$		

[a] Experimental values were obtained via analysis of VTVH-MCD data measured at the indicated probe wavelength. [b] The D and E/D values within the given ranges (or limits) provide fits of the VTVH-MCD data in which the resulting χ^2-value is ≤1.5 times the χ^2-value obtained with the "best fit" values.

high-frequency EPR (HFEPR)/MCD study of a high-spin Co(II) system.[46] The results from our VTVH-MCD data analysis for complexes **1**−**3** are summarized in Table 3.[47]

As expected on the basis of qualitative considerations, acceptable fits of the VTVH-MCD data of complex **1** could be obtained only for $D > 0$ cm^{-1}. The best overall fit of the 470 nm data set, which probes the VTVH-MCD behavior of band 1, was achieved with the following ZFS parameters: $D = +9$ cm^{-1} and $E/D = 0.20$. However, the variance of the χ^2 parameter with respect to D reveals that this optimal fit corresponds to a shallow minimum, and we can only state with certainty that $D > +4$ cm^{-1}. In contrast, the χ^2 parameter exhibits a stronger dependence on the E/D ratio, leading to acceptable fits only for moderately rhombic values (Table 3). Additionally, the best overall fits of the 470 nm VTVH data set suggest that the corresponding transition (band 1) is polarized perpendicular to the x-axis. Since this transition has predominately S→Fe(II) CT character, it should be primarily polarized along the Fe−S bond vector. Consequently, as band polarizations relate to the principal axes of the **D**-tensor of the complex, our VTVH-MCD data suggest that in **1** the Fe−S bond vector is oriented within the yz-plane of the **D**-tensor.

A similar analysis was performed on the VTVH-MCD data of complex **2**, confirming that $D < 0$ cm^{-1} (Table 3). In sharp contrast to the 470 nm band of complex **1**, the transition at 370 nm of complex **2** is predominantly z-polarized, with only marginal contributions from x- and y-polarizations. For **3**, the only acceptable fits of the 314 nm VTVH-MCD data set were found for $D > 0$ cm^{-1}, again consistent with our qualitative considerations. The best fit was obtained with $D = +6.0$ cm^{-1} and $E/D = 0.05$, although acceptable fits also resulted for ZFS parameters within the ranges $+4 < D < +11$ cm^{-1} and $0.04 < E/D < 0.15$ (Table 3). Regardless of the D and E/D values chosen, the fitting procedure consistently required that the dominant contribution to the 314 nm MCD feature involve the M_{yz} transition moment product, indicating that the corresponding transition is polarized perpendicular to the molecular x-axis.

Ligand-Binding Studies. As noted above, absorption results suggest that MeOH is capable of coordinating to the Fe(II) centers of complexes **2** and **3** (Table 1). Figure S5(a) displays the low-temperature MCD spectrum of **3** in a frozen solution of 2:1 MeOH/glycerol. Although the overall patterns of bands are similar in the solid-state and solution spectra, the bands are blue-shifted by ∼2000 cm^{-1} upon solvation of **3**. This result suggests that the binding of MeOH (or glycerol) to the Fe center is sufficiently strong to perturb the absolute band energies but not strong enough to alter the overall appearance of the spectrum (i.e., the band intensities and relative energies), which is determined primarily by the N_4S ligand set.

The VTVH-MCD saturation curves measured for **3** also exhibit significant changes upon solvation of the complex (Figure S5(b)). Compared to the solid-state data, the solution MCD magnetization curves saturate more rapidly with field and exhibit a lesser degree of nesting. Fitting of the VTVH-MCD solution data indicates that the D value increases upon solvation and that the E/D ratio approaches the rhombic limit. The best fit was obtained with $D = +12$ cm^{-1} and $E/D = 0.25$, although good fits were also found over a range of large D values ($|D| > 9$ cm^{-1}) near the rhombic limit.

For complex **3**, additional ligand-binding studies were carried out using azide, a close electronic mimic of superoxide. The results of these studies are summarized in the Supporting Information.

Computations. (a) Spin-Hamiltonian Parameters. INDO/S-CI calculations performed on complexes **1** and **2** predict ZFS values consistent with those provided by our analysis of the VTVH-MCD data (Table 3). While the computed D value for **1** ($D = +3.7$ cm^{-1}) is too small, the INDO/S-CI calculations predict a rhombic system ($E/D = 0.24$) with a positive ZFS parameter D, as determined experimentally. Interestingly, the calculations provide an unusual orientation of the **D**-tensor in which none of the principal axes are collinear with the Fe−ligand bonds. For complexes such as **1**, with approximate square-pyramidal geometry, one of the principal axes would be expected to coincide with the pseudo-C_4 axis, in this case the Fe−S bond vector. Instead, the computed **D**-tensor is rotated such that one axis forms a 24° angle with the Fe−S bond axis, while another bisects the N_{pyr}−Fe−N_{pyr} bond vectors (Figure 6). Since the Fe−S bond lies within the yz-plane of the computed **D**-tensor, this prediction is fully consistent with the VTVH-MCD polarization data presented above. This unexpected **D**-tensor orientation reflects key elements of the electronic structure of **1** that will be explored in the next section.

INDO/S-CI calculations for complex **2** provide ZFS values of $D = -4.9$ cm^{-1} and $E/D = 0.12$, reproducing the negative ZFS parameter D and moderate rhombicity determined experimentally (Table 3). Compared to complex **1**, the calculated **D**-tensor orientation of **2** is more readily understood. The z-axis lies directly along the Fe−S bond, and the nearly linear N_2−

(46) Krzystek, J.; Zvyagin, S. A.; Ozarowski, A.; Fiedler, A. T.; Brunold, T. C.; Telser, J. *J. Am. Chem. Soc.* **2004**, *126*, 2148−2155.

(47) For all three complexes, the most detailed analysis was performed on the low-energy data sets, since the high-energy data were somewhat affected by temperature-independent (***B***-term) contributions that became apparent at energies > 30 000 cm^{-1}. However, in all instances, the ZFS parameters that provided the best fits of the low-energy VTVH-MCD data sets also provided excellent fits of the corresponding high-energy data sets.

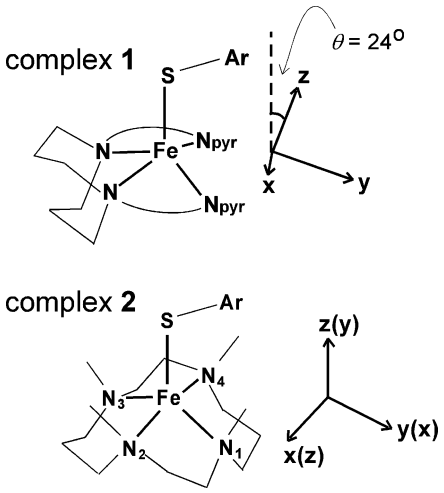

Figure 6. Structures of complexes **1** and **2** illustrating the **D**-tensor orientations provided by INDO/S-CI calculations. For **2**, the alternate coordinate system considered in our DFT studies is indicated in parentheses.

Fe−N_4 unit defines the *x*-axis (Figure 6), again consistent with our VTVH-MCD results.

Although the VTVH-MCD data unambiguously require a positive *D* value for complex **3**, INDO/S-CI calculations predict a negative *D* value of −3.8 cm^{-1} and an *E*/*D* ratio of 0.23. This discrepancy is likely due to the fact that the calculation, even after inclusion of a large CI active space, provided a ground-state Fe 3d electron configuration that is inconsistent with both our spectroscopic results and DFT calculations for **3** (vide infra).

(b) Ligand Frontier Orbitals. To identify the relevant frontier orbitals of the ligands present in complexes **1**−**3**, DFT calculations were first performed on the free L^8py_2 and Me_4-cyclam macrocycles, as well as the aryl thiolate ligands of **1** and **2**. In agreement with earlier computational studies,[48] the two highest-energy occupied MOs (HOMOs) of the aryl thiolates have primarily sulfur 3p orbital character but also possess considerable contributions from the aromatic ring (Figure 7, top). Using previously established nomenclature,[49] these thiolate π-orbitals are labeled according to their orientation with respect to the benzene ring: π_{ip} lies in the plane of the aromatic ring, while π_{op} is perpendicular to this plane. The π_{ip} and π_{op} orbitals are nearly degenerate in the isolated ligand but differ substantially with respect to the extent of electron delocalization onto the aryl ring, amounting to 30% for the π_{op} orbital, compared to only 10% for the π_{ip} orbital.

Single-point DFT calculations on the free L^8py_2 and Me_4-cyclam ligands were performed with the macrocycles in the same conformation as adopted in complexes **1** and **2**. As expected, the four highest-energy occupied MOs of both the Me_4cyclam and L^8py_2 macrocycles possess almost exclusively N_σ orbital character. Yet unlike Me_4cyclam, the L^8py_2 macrocycle features two unoccupied π*-based MOs localized on the pyridine moieties (Figure 7, bottom). These π* MOs lie only ∼18 000 cm^{-1} above the HOMO and are thus available for π-backbonding upon binding of L^8py_2 to low-valent ("electron rich") metals.

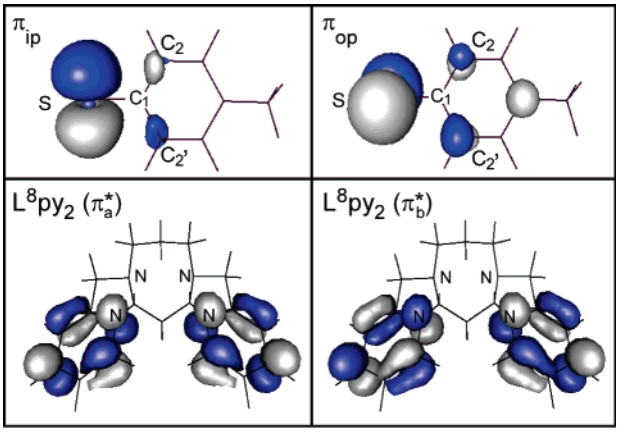

Figure 7. (Top) Isosurface plots of the π_{ip} and π_{op} MOs obtained from DFT calculations on the free *p*-tolyl thiolate ligand. (Bottom) Plots of the two lowest-energy unoccupied MOs obtained from DFT calculations on the free L^8py_2 ligand.

(c) Bonding Description for Fe(II)−Thiolate Models. Single-point DFT calculations were also performed on the full complexes **1**−**3** except for the counterions, as detailed in the Computational Methods section. Table S5 summarizes the energies and compositions of the relevant spin-down molecular orbitals for complexes **1**−**3**, and the corresponding MO energy-level diagrams are shown in Figure 8.[50]

The electronic structure of **1** was computed with the molecule aligned according to the **D**-tensor provided by INDO/S-CI calculations (vide supra), in which the *z*-axis is rotated away from the Fe−S bond vector by 24° and the *y*-axis bisects the N_{pyr}−Fe−N_{pyr} bond angle (Figure 6).[51] The reason for this unusual **D**-tensor orientation becomes apparent upon examination of the orbital compositions of the Fe d-based MOs. MOs 123 and 124 (Fe d_{xz}- and d_{yz}-based, respectively) reveal very strong bonding interactions between the Fe(II) orbitals and the π-acceptor orbitals of the L^8py_2 macrocycle, with 28% and 42%, respectively, of the electron density residing on the pyridyl rings (Table S5). This π-backbonding is also evident from MOs 126 and 127 (the antibonding counterparts of MOs 123 and 124) that, although primarily localized on the L^8py_2 ligand, contain substantial Fe d-orbital character. These results indicate that the Fe d-orbitals in complex **1** are oriented such as to maximize their π-interactions with the pyridyl acceptor orbitals. Importantly, both the orbital compositions and the **D**-tensor alignment reveal that the dominant Fe-ligand interactions in complex **1** involve the equatorial pyridyl moieties, not the axial thiolate ligand.

The computed Fe d-orbital splitting pattern for **1** is consistent with an Fe(II) system with $D > 0$ cm^{-1}, as the doubly occupied $d_{x^2-y^2}$-based MO (#122) is lower in energy than the d_{xz}/d_{yz}-

(48) McNaughton, R. L.; Tipton, A. A.; Rubie, N. D.; Conry, R. R.; Kirk, M. L. *Inorg. Chem.* **2000**, *39*, 5697−5706.
(49) Davis, M. I.; Orville, A. M.; Neese, F.; Zaleski, J. M.; Lipscomb, J. D.; Solomon, E. I. *J. Am. Chem. Soc.* **2002**, *124*, 602−614.

(50) For these $S = 2$ complexes, spin polarization lowers the energies of the majority-spin (i.e., spin-up) Fe d orbitals relative to their minority-spin (i.e., spin-down) counterparts, resulting in substantial mixing of the former with ligand-based orbitals. The natures of the Fe−ligand bonding interactions are therefore inferred from the ligand- and Fe d-based spin-down MOs that are considerably less mixed than their spin-up counterparts.
(51) Initial calculations were performed with the Fe−S bond oriented along the *z*-axis and with the four N atoms lying approximately in the *xy*-plane, accounting for the approximate C_{4v} symmetry of the complex. However, this resulted in a set of Fe d-based MOs with similar contributions from multiple d orbitals, thus complicating analysis of the electronic structure. In constrast, the orientation provided by INDO/S-CI calculations resulted in Fe d-based MOs with a single dominant contributor orbital, although some d-orbital mixing remained to maximize the bonding interactions with both the thiolate and L^8py_2-based orbitals.

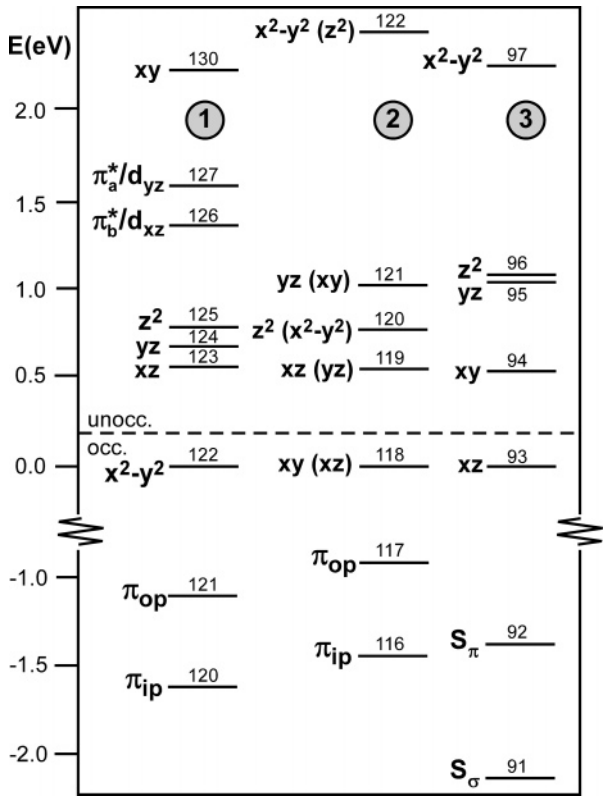

Figure 8. MO energy diagrams for complexes **1**−**3** obtained from spin-unrestricted DFT calculations, showing the energies of the spin-down MOs relative to that of the corresponding HOMO. MOs are labeled according to their principal contributors.

derived pair of MOs (#123/124), which are split by ∼1000 cm^{-1}.[52] This splitting of the d_{xz}- and d_{yz}-based MOs (ΔE_π) is responsible, in large part, for the substantial rhombicity exhibited by **1** (Table 3). The most unusual electronic feature of this complex is the 12 000 cm^{-1} energy gap (ΔE_σ) between the Fe d_{z^2}- and d_{xy}-based MOs (#125 and #130, respectively) that constitute the $e_g(\sigma^*)$ set of MOs in the parent O_h symmetry. This enormous splitting suggests that the nitrogen "lone pairs" of the L^8py_2 ligand are much better σ-donors than the axial aryl thiolate ligand.[53]

DFT studies of **2** were performed with the model aligned according to the **D**-tensor orientation provided by INDO/S-CI calculations (Figure 6). This resulted in an Fe d-orbital splitting pattern intermediate between those expected for trigonal bipyramidal and square pyramidal coordination geometries, consistent with the Fe ligand environment in complex **2** (Figure 1). In particular, the trigonal distortion exhibited by this species results in a significant destabilization of the Fe d_{yz} orbital through σ-antibonding interactions with the nitrogen-based lone pairs of the Me_4cyclam ligand and, consequently, in a 3900 cm^{-1} splitting of the Fe d_π-based MOs (#119 and 121). A more conventional splitting pattern is obtained when the *z*-axis and *y*-axis are oriented along the Fe−N_2 and Fe−S bond vectors, respectively, as shown in parentheses in Figure 6. The MO labels obtained with this coordinate system are also indicated (in parentheses) in Table S5 and Figure 8. This alternate orientation provides a d-orbital splitting pattern typical of trigonal bipyramidal systems, which are characterized by $D < 0$ cm^{-1} and d-orbital energies following the sequence (d_{xz}, d_{yz}) < ($d_{x^2-y^2}$, d_{xy}) < d_{z^2}. Since the VTVH-MCD data also indicate a negative *D* value for **2**, it appears that the "effective" electronic symmetry of this complex is indeed closer to trigonal bipyramidal than square pyramidal. Nevertheless, the Fe d-orbital labels obtained by orienting **2** according to the INDO/S-CI computed **D**-tensor will be used for the remainder of the paper.

For complexes **1** and **2** with aryl thiolates, the bonding interactions between the π_{ip} and π_{op} orbitals and the Fe d-orbitals depend on two structural parameters: (i) the Fe−S−C_1 bond angle and (ii) the Fe−S−C_1−C_2 dihedral angle (see Figure 7 for labeling scheme used). The X-ray crystal structures of complexes **1** and **2** reveal Fe−S−C_1 angles of 98° and 119°, respectively, and dihedral angles of 111° and 97°.[54] Since for both complexes the two sets of angles are much closer to 90° than 180°, the π_{op} orbital points primarily along the Fe−S bond and forms σ−bonds with the Fe d-orbitals, while the π_{ip} orbital is largely perpendicular to the Fe−S bond vector and thus develops π-bonding interactions with the Fe d-orbitals.[55] For complex **1**, the Fe−S bonding interactions primarily involve the Fe d_{xz}/π_{ip} and d_{z^2}/π_{op} orbitals, as reflected in the Fe d-based MOs 123 and 125 (Table S5). The π_{ip}-based MO (#120) is ∼4000 cm^{-1} lower in energy than the π_{op}-based MO (#121), suggesting that the Fe−S π-interaction is considerably stronger than the Fe−S σ-interaction. For complex **2**, the Fe−S bonding interactions are reflected in the Fe d-based MOs 119−121. The Fe−S σ-interaction principally involves the Fe d_{z^2} and π_{op} orbitals, while both the Fe d_{xz} and d_{yz} orbitals engage in π-interactions with the π_{ip} orbital. As with complex **1**, the Fe−S σ-interaction is much weaker than the π-interaction, which is evidenced by the fact that the Fe d_{z^2}-based MO (#120) is ∼2500 cm^{-1} lower in energy than the Fe d_{yz}-based MO (#121). Collectively, these results suggest that the aryl thiolate is a poor σ-donor, albeit an effective π-donor.

In contrast to **1** and **2**, complex **3** contains an *alkyl* thiolate ligand whose S 3p orbitals are not involved in intraligand π-interactions. For systems involving metal−(alkyl)thiolate bonds, such as the SOR, blue copper, and sulfite oxidase active sites, the nature of the metal-sulfur bonding interaction is determined by the M−S−C_1 bond angle.[56] If this angle is near 180°, then the two S 3p-based lone pairs interact with the metal d-orbitals in a π fashion, but as the bond angle is reduced from 180° to 90°, one lone pair starts developing a pseudo-σ interaction with the metal center. The crystal structure of **3** reveals an Fe−S−C_1 bond angle close to 90° (98°), suggesting that the thiolate possesses one almost purely σ-donating orbital (S_σ) and one purely π-donating orbital (S_π). Furthermore, the constraints imposed on the pendant thiolate by the cyclam ring result in a N_2−Fe−S−C_1 dihedral angle (Figure 2) of nearly 0° (3.3°). As a result, the S_π orbital interacts *exclusively* with the Fe d_{yz} orbital, while the Fe d_{xz} orbital is orthogonal to both S 3p-based lone pairs (Scheme 3). This situation is in contrast

(52) The coordinate system for complex **1** shown in Figure 6 allows for pure d_{xz} and d_{yz} orbitals but interchanges the identities of the d_{xy} and $d_{x^2-y^2}$ orbitals.

(53) Two additional factors contribute to the large ΔE_σ value for **1**: (i) the d_{z^2} orbital is not oriented directly along the Fe−S bond axis and thus does not experience the full effect of the destabilizing σ^* interaction, and (b) the pyridyl rings are tilted slightly out of the N_{pyr}−Fe−N_{pyr} plane, allowing the d_{z^2} orbital to engage in weak π-backbonding (i.e. stabilizing) interactions with the L^8py_2 π^*-acceptor orbitals.

(54) For complex **2**, the angles reported in the text are averaged over both crystallographically independent cations.

(55) Note that for both complexes deviations of these angles from 90° give rise to somewhat mixed σ- and π-bonding interactions.

(56) Solomon, E. I.; Szilagyi, R. K.; George, S. D.; Basumallick, L. *Chem. Rev.* **2004**, *104*, 419−458.

Scheme 3

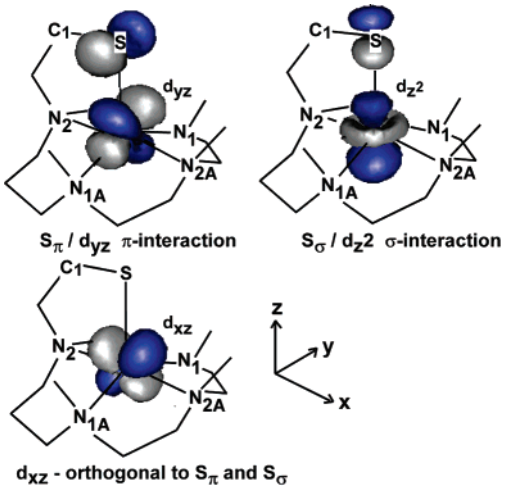

to the one encountered above for complex **2**, wherein the orientation of the untethered aryl thiolate results in significant bonding interactions between the π_{ip} orbital and both the Fe d_{xz} and d_{yz} orbitals.

The MO diagram of **3** shown in Figure 8 reflects the strong σ- and π-donating ability of the alkyl thiolate. In particular, the interaction between the S_σ and Fe d_{z^2} orbitals is very covalent, as judged on the basis of both MO energies and compositions (Table S5). While for both **1** and **2** the thiolate-based MO principally involved in Fe−S π-bonding (π_{ip}) is several thousand wavenumbers lower in energy than the corresponding σ-bonding MO (π_{op}), for **3** this pattern is reversed with the S_σ-based MO (#91) now stabilized by ∼6000 cm^{-1} relative to the S_π-based MO (#92). Furthermore, the Fe d_{z^2}-based MO (#96) of **3** is strongly destabilized relative to its counterpart in complex **2**, suggesting that alkyl thiolates are much stronger σ-donors compared to aryl thiolates. These differences between the two types of thiolate ligands are likely due to the highly delocalized nature of the π_{op} orbital in aryl thiolates (Figure 7), which prevents strong σ-bonding interactions with the Fe centers in **1** and **2**.

Our DFT results indicate that the singly occupied Fe d-based spin-down MO of **3** (#93) has primarily Fe d_{xz} character, which provides an interesting contrast to the situation encountered for complexes **1** and **2** where the corresponding MOs lie in the equatorial plane (d_{xy} or $d_{x^2-y^2}$ character). This change is due to the unique structural features of **3** described above, which ensure that the Fe d_{xz} orbital is essentially nonbonding. The computed Fe d-orbital splitting pattern for **3** provides insight into the origin of the changes in the ZFS parameters accompanying solvation of this species in MeOH. As noted above, upon weak solvent binding to the Fe(II) center of **3** the *D* value increases and the *E*/*D* ratio approaches the rhombic limit. For such tetragonal Fe(II) systems, these results suggest that the energy gap between the doubly occupied Fe d-orbital and the other d-orbitals of the parent t_{2g} set is diminished upon solvation and that the splitting pattern becomes more characteristic of a system with negative *D*.[44] This scenario is only possible if $E(d_{xz}) < E(d_{xy})$ in the solid state, since MeOH binding is expected to destabilize the d_{xz} and d_{yz} orbitals, while leaving d_{xy} largely unaffected (Figure 9).

Spectral Assignments. In light of the fact that the electronic structure descriptions of the Fe(II) models **1**−**3** provided by

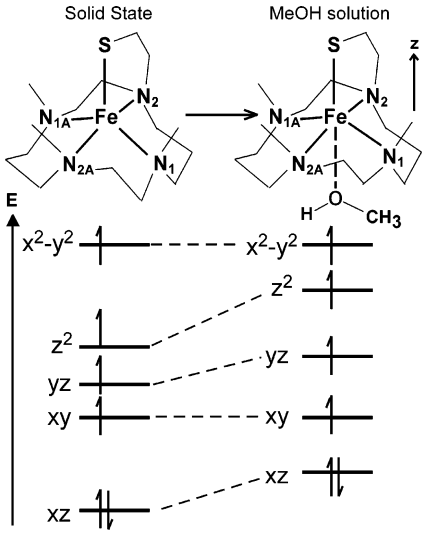

Figure 9. Qualitative energy level diagram illustrating the effect of MeOH coordination on Fe d-orbital energies of complex **3**.

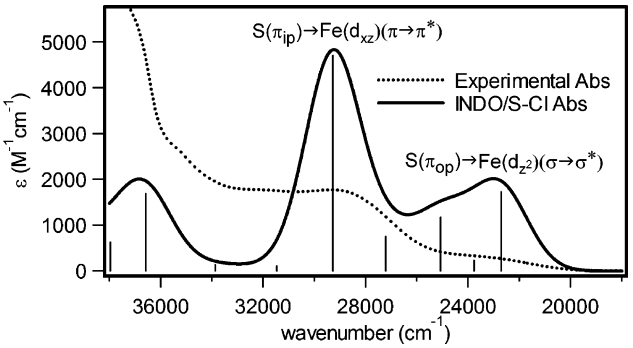

Figure 10. INDO/S-CI calculated spectrum for **1** (—) obtained using the crystallographically determined structure, along with the experimental absorption spectrum of **1** in MeCN solution at room temperature (···).

DFT and INDO/S-CI calculations appear largely consistent with our spectroscopic results, it is reasonable to use these methods for assigning key features in the corresponding electronic absorption and MCD spectra. To accomplish this goal, the INDO/S-CI method was used to interpret the absorption spectrum of complex **1**. As shown in Figure 10, the calculated absorption spectrum for **1** consists of two prominent bands that correspond to the two principal CT features in the experimental spectrum.[57] On the basis of this calculation, the low-energy feature in the experimental spectrum (bands 1 and 2) is assigned to the $S(\pi_{op})\rightarrow Fe(d_{z^2})$ ($\sigma\rightarrow\sigma^*$) CT transition, while the more intense feature at higher energy (band 6) is attributed to the $S(\pi_{ip})\rightarrow Fe(d_{xz})$ ($\pi\rightarrow\pi^*$) CT transition (see Table 2). Band 7 at 30 600 cm^{-1} is then assigned to the $S(\pi_{ip})\rightarrow Fe(d_{z^2})$ transition, where the considerable absorption intensity of this band suggests that the π_{ip} orbital experiences a significant σ-interaction with the Fe d_{z^2} orbital.[58] Note that the spectroscopically determined energy splitting of 1650 cm^{-1} between the Fe d_{xz} and d_{z^2} orbitals is in remarkable agreement with the DFT-calculated splitting of 1630 cm^{-1} (Table S5). Figure 11 (left) summarizes these

(57) The calculated spectrum in Figure 10 has been red-shifted by 4000 cm^{-1} to facilitate comparison with the experimental spectrum.

(58) It is important to note that bands that are intense in the absorption spectrum are often weak in the MCD spectrum, and it is therefore not surprising that the relative intensities of bands 6 and 7 are dramatically different in the two spectra.

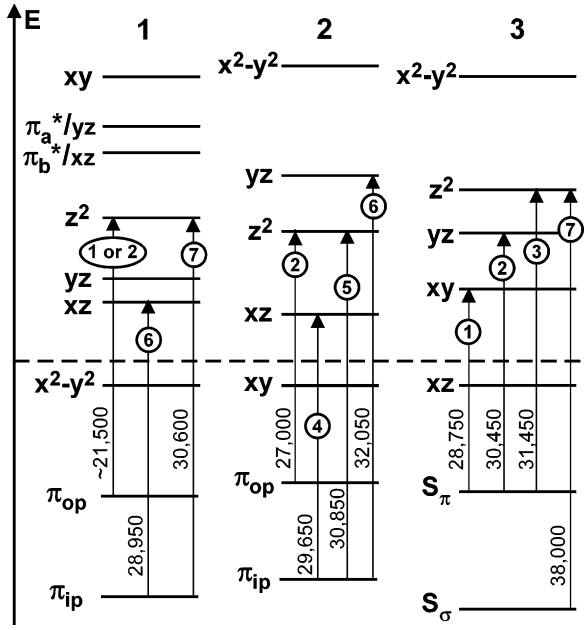

Figure 11. Energy-level diagram displaying the experimentally determined transition energies (in cm^{-1}) within the MO framework provided by DFT calculations for **1**−**3**. Transitions are labeled according to the numbering scheme used in Figure 4 and Table 2.

spectral assignments within the MO framework provided by DFT calculations for **1**.

INDO/S-CI calculations for complex **2** afforded results very similar to those discussed above for **1**, leading to closely analogous assignments of key spectral features (Figure 11, center). Specifically, the weak shoulder in the absorption spectrum, corresponding to the positive MCD feature at ~27 000 cm^{-1} (band 2), arises from the $S(\pi_{op})\rightarrow Fe(d_{z^2})$ ($\sigma\rightarrow\sigma^*$) CT transition. Note that this assignment concurs nicely with the *z*-polarization of band 2 as determined by our VTVH-MCD analysis. The intense low-temperature absorption feature at 31 100 cm^{-1} (bands 5 and 6) has contributions from two CT transitions, involving electronic excitations from the π_{ip}-based MO into the Fe d_{z^2}- and d_{yz}-derived orbitals (Figure 11). The separation of bands 5 and 6 thus provides an energy splitting of 1200 cm^{-1} between the Fe d_{z^2} and d_{yz} orbitals, which is somewhat smaller than the DFT-calculated value of 2500 cm^{-1} (Table S5).[59]

The solid-state MCD spectrum of **3** reveals that the low-energy absorption feature consists of three bands (Figure 4). As DFT calculations indicate that $E(S_\sigma) \ll E(S_\pi)$, we conclude that all three bands arise from $S_\pi\rightarrow$Fe(II) CT transitions. Band 2, which is intense in both the electronic absorption and MCD spectra, is assigned to the $S_\pi\rightarrow Fe(d_{yz})$ ($\pi\rightarrow\pi^*$) transition. The weak absorption features at 28 750 cm^{-1} (band 1) and 31 450 cm^{-1} (band 3) are assigned to the $S_\pi\rightarrow Fe(d_{xy})$ and $S_\pi\rightarrow Fe(d_{z^2})$ transitions, respectively.[60] Despite its weak absorption intensity, the $S_\pi\rightarrow Fe(d_{z^2})$ transition acquires considerable MCD intensity due to excited-state mixing via SOC with the $S_\pi\rightarrow Fe(d_{yz})$ ($\pi\rightarrow\pi^*$) transition, resulting in the pseudo-***A*** term feature centered at 30 900 cm^{-1} (Figure 4). While the three moderately intense bands that lie within the absorption feature at 35 000 cm^{-1} (bands 4−6) are difficult to assign conclusively, it is obvious that the intense band at 38 000 cm^{-1} (band 7) must arise from the $S_\sigma\rightarrow Fe(d_{z^2})$ ($\sigma\rightarrow\sigma^*$) transition. Even when accounting for the fact that this band is superimposed on the shoulder of a high-energy band with a maximum at $\gg$40 000 cm^{-1}, it remains twice as intense as the corresponding $\sigma\rightarrow\sigma^*$ transition of **2**, confirming the highly covalent nature of the Fe−S σ-bonding interaction in complex **3**.

Discussion

A more complete understanding of the catalytic activity of SORs requires the synthesis and characterization of relevant model complexes that accurately mimic the geometry, reactivity, and electronic structure of the SOR_{red} active site. This report describes the synthesis of two novel Fe(II) complexes, **2** and **3**, that possess the N_4S donor set of ligands found in SOR_{red}. Unlike the first-generation of SOR models represented by **1**, which utilizes the tetradentate ligand L^8py_2 to model the four equatorial His residues found for the enzymatic site,[18] these second- and third-generation models are based on the macrocyclic N_4-donor cyclam ligand (Scheme 1). Our X-ray crystallographic results show that the molecular structures of both **2** and **3**, unlike that of **1**, display large trigonal distortions from an idealized square-pyramidal geometry, with τ parameters in the range of 0.46 to 0.57. The three complexes also differ with respect to the nature and position of the axial thiolate ligand. While **1** and **2** feature unconstrained aryl thiolates, complex **3** contains an alkyl thiolate that is tethered to the cyclam ring (Figure 2), resulting in a restricted thiolate orientation.

To explore the electronic structures of models **1**−**3** in detail, we have employed electronic absorption, MCD, and VTVH-MCD spectroscopies in conjunction with DFT and INDO/S-CI calculations. By combining the insights gained from our electronic structure calculations with the results obtained from our spectroscopic studies, we have succeeded in developing experimentally validated bonding descriptions for all three complexes. These bonding descriptions greatly enhance our understanding of the dominant Fe(II)−thiolate bonding interactions in SOR_{red}-like species, as well as their dependencies on the identities of the equatorial N-donor ligands.

Comparisons to SOR Active Site. Like the enzymatic system, all three generations of SOR models included in this study feature a N_4S ligand set around a high-spin ($S = 2$) Fe(II) center, and also exhibit vacant coordination sites trans to the thiolate ligand.[4−6] The first-generation of models (**1**) provide the best structural mimics of SOR_{red}, as the Fe(II) coordination environment is clearly square-pyramidal ($\tau \approx 0.15$). In contrast, the Fe(II) coordination environment in the second- and third-generation models is intermediate between square-pyramidal and trigonal-pyramidal ($\tau \approx 0.50$).

Although complex **1** is *structurally* the best model of the SOR_{red} active site, the spectroscopic and computational results

(59) Based on our INDO/S-CI computations, the $S(\pi_{ip})\rightarrow Fe(d_{yz})$ ($\pi\rightarrow\pi^*$) transition is strongly polarized along the Fe−S bond (*z*-axis), while the $S(\pi_{ip})\rightarrow Fe(d_{z^2})$ transition is polarized along the *y*-axis. Mixing of the corresponding excited states via spin−orbit coupling (SOC) should thus give rise to a pseudo-***A*** term feature, which is indeed observed in the MCD spectrum of **2** at 31 500 cm^{-1} (Figure 4).

(60) Based on these assignments, it appears that the DFT calculation for **3** underestimates the splitting between the Fe d_{yz}- and d_{z^2}-based MOs (#95 and #96, respectively, in Figure 8/Table S3), which is found to be 1000 cm^{-1} experimentally, as compared to 160 cm^{-1} predicted computationally. Moreover, the 1700 cm^{-1} experimental splitting between the Fe d_{xy}- and d_{yz}-based MOs (#94 and #95, respectively) is much smaller than the calculated splitting of 4020 cm^{-1}. It is therefore apparent that, although DFT provides a qualitatively correct Fe d-orbital splitting pattern for **3**, the experimental Fe d-orbital splitting pattern is, in fact, reminiscent of an "effective" electronic symmetry intermediate between trigonal bipyramidal and square pyramidal.

presented herein indicate that *electronically* it differs quite substantially. This difference is evident even on a qualitative level; namely, while SOR_{red} (as well as complexes **2** and **3**) is colorless,[6] **1** exhibits a bright yellow color both in the solid state and in solution due to the presence of S→Fe(II) CT transitions in the visible region. Expressing this observation in quantitative terms, the onset of the CT manifold appears at ~29 000 cm^{-1} in the SOR_{red} absorption spectrum[6] but at an energy of ~20 000 cm^{-1} in the spectrum of complex **1**. S→Fe(II) CT transitions formally produce an Fe(I) center in the excited state, and since this low Fe oxidation state is highly unstable in most coordination environments, these transitions normally appear far in the UV region. However, our spectroscopic and computational studies of complex **1** have revealed strong bonding interactions between the Fe(II) d_π orbitals and the pyridine π^* orbitals, which allow for a ~4000 cm^{-1} stabilization through π-backbonding of the transiently formed Fe(I) center in these CT excited states. This result has implications for the competence of **1** as a functional SOR mimic, since it is widely believed that the *destabilization* of the Fe d_π orbitals via Fe−S π-antibonding interactions is crucial for facile electron transfer to the superoxide anion.[14] In the SOR_{red} active site, such a stabilization of the Fe d_π orbitals via π-backbonding is not possible, as the imidazole rings of the His residues are weak π-*donor* ligands,[61] not π-acceptors such as L^8py_2.

The Fe d-orbital splitting pattern determined for **1** is consistent with both the square-pyramidal coordination geometry of this complex and the positive *D* value found through analysis of VTVH-MCD data. An interesting aspect of the electronic structure of **1**, as elucidated by our DFT calculations, is the large energy gap between the Fe d_{z^2}- and d_{xy}-based MOs, ΔE_σ(**1**) = 11 800 cm^{-1}. Near-IR MCD studies by Johnson and coworkers have provided a ΔE_σ value for SOR_{red} in the range 7400 to 9000 cm^{-1}.[6] The fact that $\Delta E_\sigma(SOR_{red})$ is significantly smaller than ΔE_σ(**1**) initially appears somewhat surprising, given that the Fe−S bond distance in the protein is larger than that in the model; i.e., r(Fe−S) = 2.32 Å for **1**,[18] as compared to r(Fe−S) = 2.42 Å (X-ray structure[4]) or 2.37 Å (EXAFS[6]) for SOR_{red}. However, these ΔE_σ values are consistent with our spectroscopic and computational results that consistently indicate that the aryl thiolate ligand of **1** is a relatively poor σ-donor compared to the alkyl thiolate found in the SOR_{red} active site.

Interestingly, the energies and intensities of some of the S→Fe(II) CT transitions of complex **2** compare quite favorably with those reported for SOR_{red}. Most notably, the S(π_{ip})→Fe(II) ($\pi\rightarrow\pi^*$) transition that occurs at 32 050 cm^{-1} (ϵ = 2470 M^{-1} cm^{-1}) for **2** resembles the prominent S→Fe(II) ($\pi\rightarrow\pi^*$) transition at 31 200 cm^{-1} ($\epsilon \approx$ 2000 M^{-1} cm^{-1}) for SOR_{red}.[6] Despite this similarity, the coordination geometry of **2** deviates substantially from square pyramidal, profoundly affecting the electronic structure and, in turn, the ZFS parameters of this complex. Our VTVH-MCD analysis reveals a negative *D* value of ~ −9 cm^{-1} for **2**, in contrast to the positive *D* value of ~ +10 cm^{-1} reported for SOR_{red}.[6] This difference can be understood in terms of the Fe d-orbital splitting pattern obtained for **2** in the alternate coordinate system, (d_{xz}, d_{yz}) < ($d_{x^2-y^2}$, d_{xy}) < d_{z^2}, which is characteristic of a system with trigonal bipyramidal geometry (Figure 6). Likewise, the trigonal distortion exhibited by complex **3** gives rise to certain electronic features that may not be shared by the enzyme active site; most importantly, a significant stabilization of the doubly occupied, "redox active" Fe d_{xz}-based MO (#93) relative to the other Fe d-based MOs, leading to a value of ΔE_π in excess of 2000 cm^{-1}. When Fe(II) exists in a more rigorous square-pyramidal coordination environment, as exemplified by complex **1** and the SOR_{red} active site, the redox active MO lies in the equatorial plane defined by the N ligands, and the value of ΔE_π is much smaller than that for **3**.[12]

Although **2** and **3** share many key structural features, the electronic properties of the two complexes are in fact quite distinct. Specifically, while **2** fails to reproduce several key elements of the electronic structure of SOR_{red}, our spectroscopic and computational results suggest that complex **3** adequately models the Fe−S bonding interactions present in the SOR active site. These similarities between **3** and SOR_{red} become particularly apparent when one compares their electronic absorption and MCD spectra. Both species exhibit multiple S→Fe(II) CT transitions, one group carrying moderate intensity ($\epsilon \approx$ 2000 M^{-1} cm^{-1}) near 31 000 cm^{-1} (30 450 cm^{-1} for **3** and 31 200 cm^{-1} for SOR_{red}) that are assigned to $\pi\rightarrow\pi^*$ transitions, and another group near 38 500 cm^{-1} (38 000 cm^{-1} for **3** and 38 900 cm^{-1} for SOR_{red}) arising from $\sigma\rightarrow\sigma^*$ CT transitions.[6] Thus, complex **3** almost quantitatively reproduces the S→Fe(II) CT energies of SOR_{red} and, unlike **1** and **2**, also yields the proper ordering $E(\sigma\rightarrow\sigma^*) \gg E(\pi\rightarrow\pi^*)$ found for the enzyme active site. Furthermore, the ΔE_σ(**3**) value of 9500 cm^{-1} is near the range of 7400 to 9000 cm^{-1} reported for SOR_{red}.[6]

Our studies permit identification of two structural features of model **3** that make its electronic properties similar to those of SOR_{red}: (i) the presence of an alkyl thiolate instead of an aryl thiolate as in **1** and **2** and (ii) the geometric constraints imposed on the thiolate orientation by the intramolecular $-CH_2-CH_2-$ linkage to the cyclam ring, which results in an Fe−S−C_1 angle of 98° and a N_2−Fe−S−C_1 dihedral angle of 3° (Figure 2). As noted above, this orientation of the thiolate ligand leads to a highly covalent Fe−S σ-bonding interaction and limits the π-bonding interaction to a single Fe d_π-orbital, causing a substantial splitting (ΔE_π) between the two Fe d_π orbitals. Given the striking electronic similarities between **3** and SOR_{red}, it is not surprising that crystallographic studies[4] have revealed that the SOR_{red} active site adopts a similar geometry with respect to the Fe−thiolate unit, with an Fe−S−C_1 angle of 116° and a N(His_{16})−Fe−S−C_1 dihedral angle of 6°, averaged over the crystallographically inequivalent protein subunits.[62] This orientation of the active-site Cys residue largely restricts the π-bonding interaction to a single Fe d_π-orbital, likely resulting in a substantial ΔE_π splitting for SOR_{red}. Collectively, the structural and spectral parallels between **3** and SOR_{red} indicate that the Fe−S bonding interactions in these two species are quite similar.

Most discussions of the electronic structure of the SOR_{red} active site have focused on the Fe(d_π)−S_π interaction, which is presumed to facilitate electron transfer from the Fe(II) center to the π^*-acceptor orbital of the substrate superoxide and

(61) (a) Holm, R. H.; Solomon, E. I. *Chem. Rev.* **1996**, *96*, 2237−2237. (b) Guckert, J. A.; Lowery, M. D.; Solomon, E. I. *J. Am. Chem. Soc.* **1995**, *117*, 2817−2844.

(62) In the crystal structure of the homotetrameric SOR from *P. furiosus*, two of the subunits (B and C) suffered from low Fe occupancies and provided less accurate active-site geometries. Thus, the bond angles reported in the text were obtained by examination of only the A and C subunits of SOR_{red} (see ref 4).

promote dissociation of the nascent peroxide anion via a trans influence.[7,14] This emphasis on the Fe−S π-interaction as being instrumental for SOR function largely stems from the fact that the absorption spectrum of the oxidized form of SOR (SOR_{ox}) is dominated by an intense S→Fe(III) CT transition of $\pi\rightarrow\pi^*$ character at ∼15 000 cm^{-1}, while the $\sigma\rightarrow\sigma^*$ counterpart is hidden under the broad absorption feature at ∼30 000 cm^{-1}.[6] Consequently, the importance of the Fe−S σ-interaction has been largely ignored in discussions of electronic-structure contributions to SOR function. Yet our spectroscopic and computational studies of complex **3**, an excellent model of SOR_{red} with respect to Fe(II)−S bonding, suggest that the Fe−S σ-interaction in SOR_{red} is likely to be even stronger and more covalent than the corresponding π-interaction. In particular, the specific orientation of the Cys residue within the SOR active site, which leads to an Fe−S−C_1 angle (116°) much closer to 90° than 180°, appears designed to maximize the σ-donor ability of the thiolate ligand. Together, these strong σ- and π-bonding interactions result in substantial charge donation from the anionic thiolate ligand to the Fe(II) center, lowering the effective nuclear charge and, thus, decreasing the redox potential ($E°$) of the Fe center in SOR. Consequently, SOR may be viewed as another member of the family of metal−thiolate containing proteins (such as blue copper[56] and sulfite oxidase[48,63]) for which the exact positioning of the cysteine residue with respect to the metal center is crucial for optimal enzymatic activity.

The SOR catalytic cycle is believed to proceed through an inner-sphere mechanism, in which the superoxide anion first binds directly to the Fe(II) center (step 1), followed by electron transfer (ET) to the substrate (step 2). For step 2 to proceed rapidly, the singly occupied π^* acceptor orbital of $O_2^{\bullet-}$ must interact electronically (via orbital overlap in a π-fashion) with the "redox-active" donor d-orbital(s) of the Fe(II) center. It has been previously suggested that the Fe d_π orbital that participates in the strong Fe−S π-interaction serves as the redox-active orbital.[7,14] However, since this orbital (d_π/S_π) is singly occupied in the SOR_{red} active site, its direct involvement in ET to the substrate would initially produce a high-energy Fe(III) $S = {}^3/_2$ intermediate (Figure 12a). To avoid such an unfavorable intermediate-spin state, the redox-active orbital of SOR_{red} would need to be the doubly occupied Fe d_{xy}-based MO, although this orbital lacks the proper orientation for significant overlap with the superoxide π^* acceptor orbital. An additional possibility, shown in Figure 12b, involves transfer of the spin-down (β) Fe electron from the d_{xy} orbital via one of the d_π orbitals (superexchange mechanism).[64] Efficient mixing between d_{xy} and the relevant d_π orbitals would require these orbitals to be in close energetic proximity. Indeed, the position of the Cys residue within the SOR_{red} active site appears to promote this type of mechanism because, as noted above, the S_π orbital is essentially orthogonal to one of the Fe d_π orbitals, a configuration that maximizes ΔE_π while minimizing the energy gap between d_{xy} and the lowest-energy d_π orbital. Thus, the axial thiolate ligand is able to depress the enzymatic redox potential via strong Fe−S π- and σ-interactions without discouraging inner-sphere electron transfer to the superoxide π^* acceptor orbital.

It is interesting to note that while the SOR active site is located near the protein surface and thus exposed to solvent,

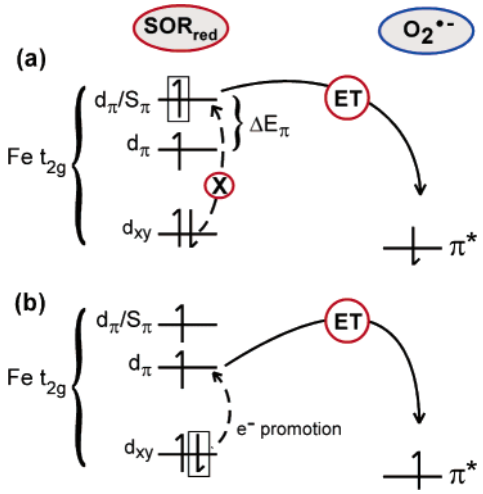

Figure 12. Two possible scenarios for inner-sphere electron transfer (ET) from the Fe(II) center of SOR to the superoxide radical ($O_2^{\bullet-}$). (a) The "boxed" electron in the Fe d_π/S_π orbital is transferred to the π^* acceptor orbital of $O_2^{\bullet-}$, yielding an Fe(III) $S = {}^3/_2$ intermediate. (b) Orbital mixing "promotes" the boxed electron from the d_{xy} orbital to the nearby d_π orbital, followed by ET to $O_2^{\bullet-}$. This mechanism directly results in the $S = {}^5/_2$ state of the oxidized enzyme.

crystallographic data indicate that the pentacoordinate Fe(II) center in SOR_{red} does not bind an axial water molecule,[4,5] and a computational study predicted a lengthy Fe−O(H_2) bond of 2.8 Å.[12] These observations can be rationalized in terms of a thiolate trans influence; i.e., for solvent to coordinate to the Fe center, it would have to develop bonding interactions with the Fe d_π and d_σ orbitals already involved in Fe−S bonding. The Fe−S σ-interaction likely plays the dominant role in modulating the affinity of the Fe center toward exogenous ligands, because, unlike the π-interaction, it is directed along the Fe−S bond and discourages σ-donating ligands, such as H_2O, from binding. In our studies, the trans influence associated with the strong Fe−S σ-interaction is evident in the weak affinity of the Fe(II) center of complex **3** toward solvent and azide, as determined spectroscopically. By analogy, the thiolate trans influence may also labilize the Fe(III)−peroxide interaction after the electron is transferred to coordinated superoxide. Specifically, the strong Fe−S(Cys) bonding interaction may weaken the Fe(III)−OO(H) bond and thus ensure rapid enzymatic turnover by facilitating H_2O_2 dissociation (step 3 of the catalytic cycle).

Conclusion

In this study we have prepared and thoroughly characterized a series of Fe(II)−thiolate complexes, **1**−**3**, that possess various types of axial thiolates (aryl and alkyl), equatorial N_4-macrocycles (L^8py_2 and Me_4cyclam), and coordination geometries. This approach permitted us to probe the influence of each of these variables on the overall electronic properties of these SOR_{red} models, with a particular focus on the nature of the Fe(II)−S bonding interactions. On the basis of our spectroscopic and computational analyses, we conclude that all three complexes mimic important features of the electronic structure of SOR_{red}, with complex **3** replicating the Fe−S bonding interactions present within the reduced active site particularly well. This similarity between complex **3** and SOR_{red} is due, in large part, to the constrained orientations of the pendant alkyl thiolate ligand in the synthetic model and the cysteine residue in the enzyme.

(63) McNaughton, R. L.; Helton, M. E.; Cosper, C. A.; Enemark, J. H.; Kirk, M. L. *Inorg. Chem.* **2004**, *43*, 1625−1637.
(64) Newton, M. D. *Chem. Rev.* **1991**, *91*, 767−792.

Acknowledgment. This research was supported by grants from the National Science Foundation (CHE-0243951 to J.A.H.), the Camille and Henry Dreyfus Foundation (Henry Dreyfus Teacher-Scholar Award to J.A.H.), the University of Wisconsin-Eau Claire, the University of Wisconsin and the Sloan Foundation Research Fellowship Program (T.C.B.), and the NSF Graduate Research Fellowship Program (A.T.F.). We thank Dr. Victor G. Young (University of Minnesota) for his assistance with the structure determination of **3**.

Supporting Information Available: X-ray crystallographic data for **2** and **3** (Table S1), relevant structural parameters for **2** and **3** (Table S2), Cartesian coordinates for DFT geometry-optimized models of **2** and **3** (Tables S3 and S4, respectively), energies and compositions of relevant molecular orbitals from DFT calculations for complexes **1**−**3** (Table S5), electronic absorption spectra in MeOH solution (Figure S1), low-temperature solid-state absorption spectra (Figure S2), Gaussian-resolved solid-state absorption spectra (Figure S3), and high-energy VTVH-MCD data sets (Figure S4) for all three complexes **1**−**3**, MCD spectra of **3** in MeOH solution (Figure S5), results from azide-binding experiments, INDO/S-CI active spaces, and complete crystallographic data for **2** and **3** in CIF format. This material is available free of charge via the Internet at http://pubs.acs.org.

JA046939S